Ridge Waves

by

Stephanie A. Harrington

B.S., University of Washington (1993)

Submitted to the Massachusetts Institute of Technology/Woods Hole Oceanographic Institution Joint Program in Physical Oceanography in partial fulfillment of the requirements for the degree of

Master of Science

at the

MASSACHUSETTS INSTITUTE OF TECHNOLOGY

and

WOODS HOLE OCEANOGRAPHIC INSTITUTION

June 1997

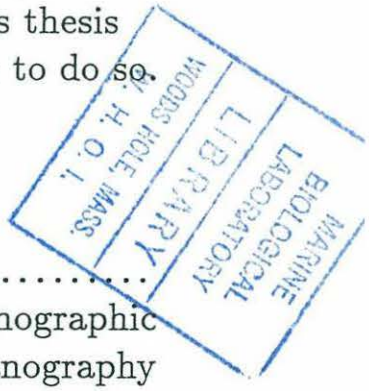

Author .....
Massachusetts Institute of Technology/Woods Hole Oceanographic Institution Joint Program in Physical Oceanography
May 16, 1997

Certified by .....
Terrence M. Joyce
Senior Scientist
Thesis Supervisor

Accepted by .....
Paola Malanotte-Rizzoli
Chair, Joint Committee for Physical Oceanography
Massachusetts Institute of Technology
Woods Hole Oceanographic Institution

Ridge Waves

by

Stephanie A. Harrington

Submitted to the Massachusetts Institute of Technology/Woods Hole
Oceanographic Institution Joint Program in Physical Oceanography
on May 16, 1997, in partial fulfillment of the
requirements for the degree of
Master of Science

Abstract

Second-class wave propagation along mid-ocean ridges is investigated in an effort to explain subinertial peaks found in the velocity spectra over the Juan de Fuca Ridge (JdFR, 4 days) and the Iceland-Faeroe Ridge (IFR, 1.8 days). Topographic cross sections of the ridges are fit by a double-exponential depth profile and the linearized shallow water equations are solved with the simplified topography. In the northern hemisphere the western ridge flank supports an infinite set of modes for a topographically trapped northward propagating wave and the eastern flank supports southward propagating modes. The eigenfunctions are calculated and dispersion curves are examined for a variety of ridge profiles. Increasing the slope of a ridge flank increases the frequencies of the modes it supports. In addition, the waves travelling along the flanks 'feel' the topography of the opposite side so that increasing the width or steepness of the eastern slope decreases the frequencies of the modes supported by the western side (and vice versa). The dispersion characteristics of the trapped nondivergent oscillations allow a zero group velocity (ZGV) so that energy may accumulate along the ridge as long as the ridge does not approach the isolated shelf profile. Including divergence lowers the frequencies of the longest waves so that a ZGV may be found for all ridge profiles. The nature of the effects of stratification, represented by a two-layer model, are explored by a perturbation procedure for weak stratification. The $\mathcal{O}(1)$ barotropic basic state is accompanied by an $\mathcal{O}(\epsilon^2)$ baroclinic perturbation. The frequencies of the barotropic modes are increased and the velocities are bottom-trapped. For reasonable values of stratification, however, this effect is small. Plugging the JdFR topography into the models produces an approximate 4-day ZGV wave with wavelengths between 1500 and 4500 km. The IFR oscillation, however, appears to be better modelled by a topographic-Rossby mode model. (Miller *et al.*, 1996) The ridge wave models discussed here also predict the observed anticyclonic velocity ellipses over the ridge and horizontal decay away from the ridge crest.

Thesis Supervisor:
Terrence M. Joyce , Senior Scientist

Acknowledgments

Although I could thank a great many people for their support during this project, I would like to thank a few in particular for their influences on this paper. My advisor Terry Joyce guided me through this problem with patience. François Primeau helped me to implement the shooting method used in Chapter 3. Karl Helfrich was always willing to answer my questions. Albert, Lou and Brian never let me down if I needed a distraction. In addition, I would also like to thank Michael and my parents for their steadfast support and faith in my abilities.

I have been supported during this research by an ONR fellowship, for which I am grateful. The impetus to this work and the ADCP data were provided by an NSF grant (OCE-9215342).

Contents

List of Figures

Chapter 1

Introduction

Idealized models of topographically trapped waves have been developed for a variety of topographic features: continental shelves (Buchwald and Adams, 1968), trenches (Mysak *et al.*, 1979), escarpments (Longuet-Higgins, 1968), islands and seamounts (Rhines, 1969b), etc. The goal of this study is to combine the methods and results of such previous work and adapt them to mid-ocean ridge topography so that the physics of low-frequency free waves particular to ridges may be explored.

Previous investigations of second-class waves over ridges include studies by Rhines (1969), Allen and Thomson (1991), and Miller *et al.* (1996). Rhines (1969a), in a study of quasigeostropic waves, includes ridge topography as an example of a topographic profile that might support internal reflections, trapping forced motions. Allen and Thomson (1991) look at bottom-trapped motions over ridges in a stratified environment where topographically trapped waves are generated by a current with a nonzero cross-ridge component. Miller *et al.* (1996) model an observed topographic mode resonance over the Iceland-Faeroe Ridge using the unforced, undamped, barotropic shallow-water equations with a rigid lid over realistic topography. In addition, Brink (1983) examines low-frequency free wave motions over a submarine bank whose topographic structure is similar to that of the idealized mid-ocean ridge used here. He briefly discusses free, inviscid wave solutions over a bank using the long-wave approximation, but focuses on the complicating effects of bottom friction and wind forcing.

Many aspects of this work will be a simplification of the previous studies. The simplifications lead to a more basic understanding of how waves trapped to ridges are affected by the various parameters that determine the shape of the ridge.

1.1 Topographically trapped waves

Topographically trapped waves are similar to planetary (or Rossby) waves in that they owe their existence to the conservation of potential vorticity. In the absence of non-conservative forces, the conservation of potential vorticity in a rotating fluid can be expressed as

$$\frac{D_h}{Dt}\left(\frac{\zeta + f}{H}\right) = 0, \tag{1.1}$$

where

$$\frac{D_h}{Dt} \equiv \frac{\partial}{\partial t} + u\frac{\partial}{\partial x} + v\frac{\partial}{\partial y},$$

ζ is the vertical component of the relative vorticity, f is the vertical component of the planetary vorticity, and H is the depth of the fluid. The planetary vorticity at a mid-latitude λ can be approximated as $f = f_0 + \beta y$, where $f_0 = 2\Omega \sin(\lambda)$ is the reference Coriolis parameter and $\beta y = 2\Omega R_e^{-1} \cos(\lambda) y$ represents a linear variation in the north-south direction. Ω is the angular rotation frequency of the earth and R_e is its radius.

In a flat-bottomed ocean f, and therefore ζ by virtue of (1.1), is changed by any perturbation in the north-south direction. A planetary wave is set up as fluid displaced toward the equator gains positive relative vorticity (cyclonic rotation) and fluid displaced poleward gains negative relative vorticity (anticyclonic rotation).

In the presence of topography perturbations up or down a topographic slope must be considered as well. From (1.1) it can be shown that a displacement into deeper water generates a gain of positive relative vorticity and a displacement into more shallow water yields a gain of negative relative vorticity. A low-frequency wave is then set up whose similarity to the planetary wave discussed above leads to it being called a topographic planetary (Rossby) wave.

There are several features ubiquitous to topographic planetary waves. It can be shown that unforced topographically trapped waves which propagate along monotonic depth profiles always propagate with the shallow water on their right (left) in the northern (southern) hemisphere. It has also been found that the amplitude of such waves decreases sharply away from the topographic features which support the waves.

Huthnance (1975) demonstrates another important attribute of topographic waves. He shows that for topography where $(\nabla H/H)$ is bounded, the group velocity must change sign at some point in frequency-wavenumber space. Thus, while phase propagation is still possible at this point, the group velocity goes to zero and the energy at this frequency and wavenumber may accumulate. The possibility of a zero group velocity will be the primary mechanism for energy accumulation explored here. A peak in energy could also occur because specific wavelengths will circumscribe discrete topographic features in an integral number of wavelengths, creating a resonant oscillation. This second process for trapping energy will be discussed further in Chapter 5.

The relative contributions of the topographic and planetary effects must be determined before either may be ignored. Rhines (1969a) compares the influences of topography and β for depth variations in one direction on a β-plane. He finds that for a simple slope where $\nabla H/H$ = constant, the predominance of topographic over planetary wave dynamics occurs at $|\nabla H| \geq H/R_e$, where R_e is the radius of the earth. As the slopes of most mid-ocean ridge more than fulfill this requirement, the planetary effect will be neglected for this study so that the influence of topography may be isolated. It must be noted, however, that β does eventually become important for very large wavelengths ($>$ 10,000 km).

1.2 Waves trapped to ridges

Because the depth of the ocean increases to either side of a mid-ocean ridge axis, an infinite set of topographic planetary wave modes is possible on both sides of the ridge. On a ridge in the northern (southern) hemisphere topographically trapped waves will

propagate to the north (south) on the western ridge slope and to the south (north) on the eastern slope.

The evidence that supports the existence of such ridge waves, and the motivation behind this study, is a subinertial signal found in the velocity spectra over several ridges. A four-day oscillation is seen in the velocities over the Juan de Fuca Ridge (Cannon and Pashinski, 1992; Cannon and Thomson, 1996), while a 1.8 day signal is found over the Iceland-Faeroe Ridge (Miller *et al.*, 1996).

An example of such a signal can be seen in the velocity spectra obtained from an ADCP moored on the southern Juan de Fuca Ridge (JdFR) from April to September, 1995. The topography of the 450 km ridge located off the coast of Oregon is shown in Figure 1-1. Although numerous seamounts and other small-scale topograpic features are present along the full length of the ridge, the general increase in depth to either side of the ridge axis dominates the topography.

The cross-rotary power spectra of the velocities over the ridge are shown in Figure 1-2. A primarily anticyclonic, low-frequency signal centered around four days is evident as far as several hundred meters above the bottom. The broad four-day peak has been observed at both the southern end of the JdFR (Cannon *et al.*, 1991) as well as the northern end (Thomson *et al.*, 1990). The characteristics of the observations from both studies, separated by about 380 km, include a maximum amplitude at the crest decreasing in both the horizontal and vertical directions, clockwise rotation, intermittency, and winter intensification. In addition, northward phase propagation is seen when observations from the two studies during concurrent measurements in 1984-85 and 1986-87 are combined (Cannon and Thomson, 1996). The observations are thought to be explained by an external source, possibly atmospheric forcing, pumping energy into the ocean to excite motion along the ridge. The energy quickly propagates away from the ridge, except at the resonancelike group velocity minimum where the energy will accumulate and become manifest in the observed velocity spectra (Chave *et al.*, 1989).

While the model of Allen and Thomson (1991) predicts the anticyclonic rotation and the increased velocity amplitude with proximity to the ridge crest, the response to

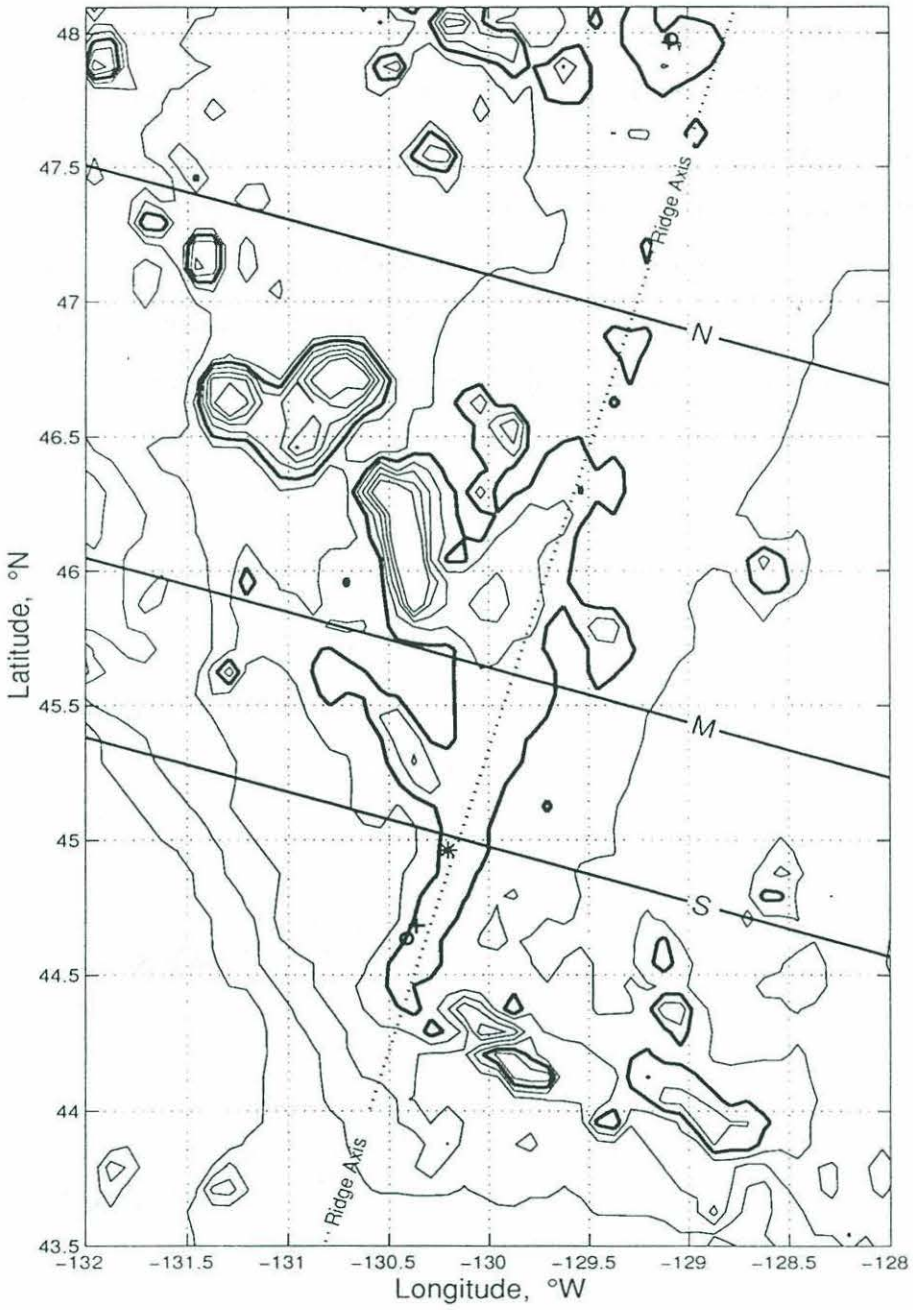

Figure 1-1: The topography of the Juan de Fuca Ridge in 250 m intervals. The bold line is 2500 m depth. The '*' near the intersection of the ridge axis and the cross-secion 'c' marks the location of the ADCP mooring used for the velocity data used in Figure 1-2. The 'o' and '+' near 48° N are the locations of the Thomson *et al.* (1990) 1984 and 1986 current meter moorings, respectively. The 'o' and '+' near 44.7° N are the locations of the Cannon *et al.* (1991) 1984 and 1986 current meter moorings, respectively.

a periodic barotropic flow across the ridge is a standing wave and phase propagation along the ridge is not possible. Rhines (1969) and Brink (1983) both predict phase propagation in opposite directions on either side of the ridge (bank), but make a long-wavelength assumption and do not explore the behaviour of shorter waves or the group velocity mimimum. (Brink does note, however, that long and short waves have group velocities in opposite directions.) The model developed here is an attempt to reproduce all of the observed features of ridge waves: the anticyclonic rotation over the ridge crest, the phase propagation along the ridge, and a group velocity mimimum in particular.

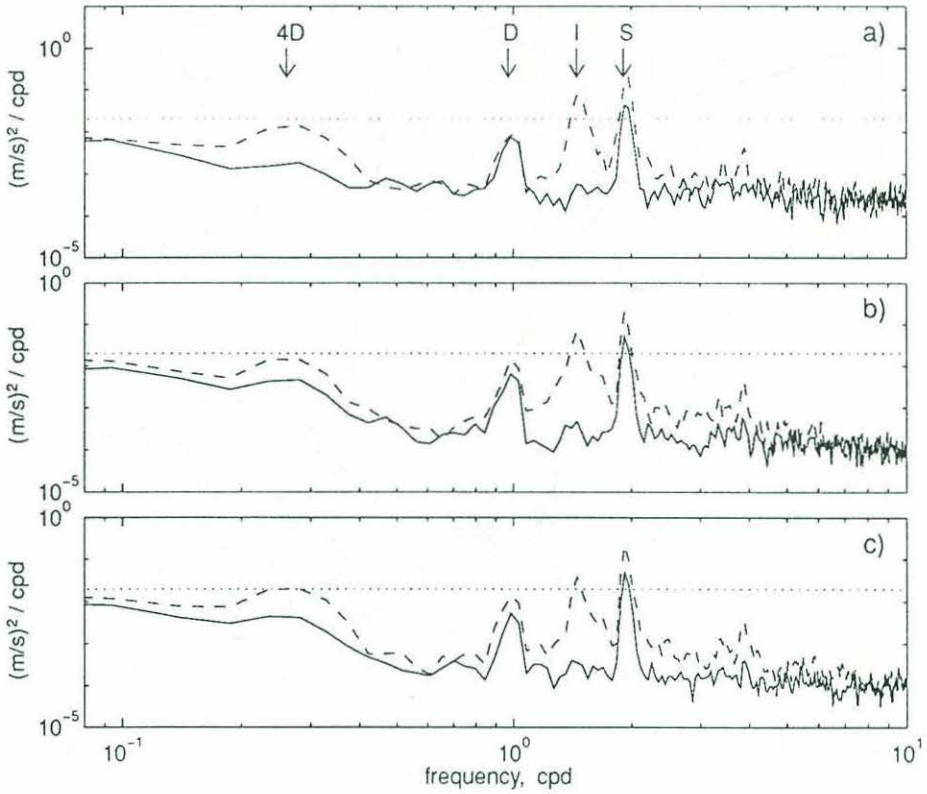

Figure 1-2: The normalized power spectra for the anticyclonic (– –) and cyclonic (—-) components of velocity measurements obtained from an ADCP moored on the Juan de Fuca Ridge. (The mooring location is shown in Figure 1-1.) The velocities are from various heights above the bottom: a) 252 m, b) 140 m, and c) 28 m. The semidiurnal (S), inertial (I), diurnal (D), and four-day (4D) oscillations are labelled.

1.3 Topographic model approximation

The investigation of topographically trapped free waves which propagate along ridges benefits tremendously by the representation of mid-ocean ridge topography by a simple depth profile. Although the length of the JdFR is finite and relatively short, the topography is assumed to be independent of y and is approximated by the double-exponential depth profile,

$$H(x) = \begin{cases} H_0 e^{(2\alpha_1 L_1)}, & -\infty < x \leq -L_1 \\ H_0 e^{(-2\alpha_1 x)}, & -L_1 \leq x \leq 0 \\ H_0 e^{(2\alpha_2 x)}, & 0 \leq x \leq L_2 \\ H_0 e^{(2\alpha_2 L_2)}, & L_2 \leq x < \infty \end{cases} \tag{1.2}$$

shown in Figure 1-3. The origin ($x = 0$) is set at the ridge axis. The exponential form of the depth profile is chosen so that many of the calculations in the following chapters are simplified.

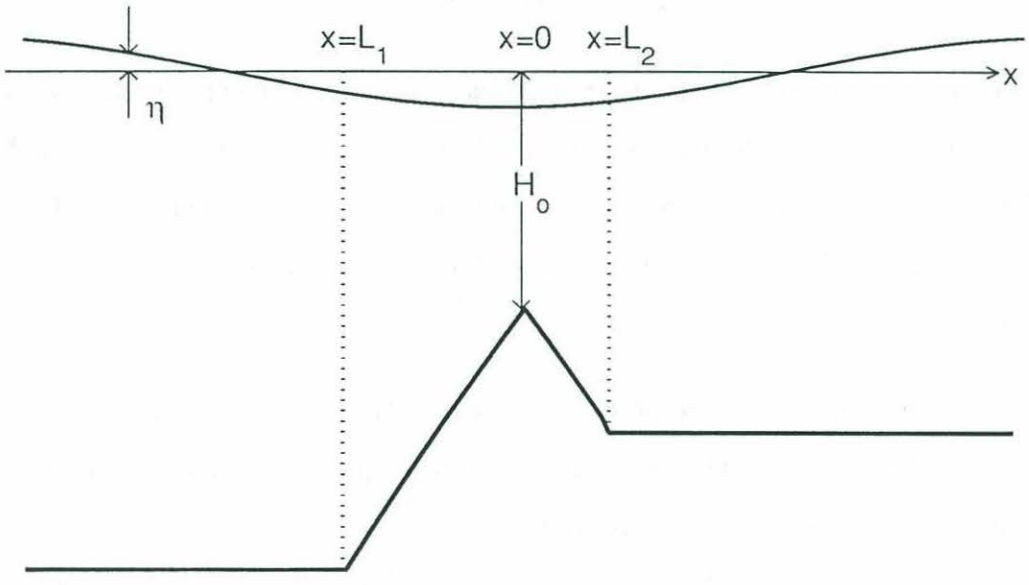

Figure 1-3: The double-exponential topographic model configuration used to explore ridge waves.

The coordinate system of the JdFR is rotated so that the ridge axis is defined as the y-axis and the three ridge cross sections marked on Figure 1-1 are fit with

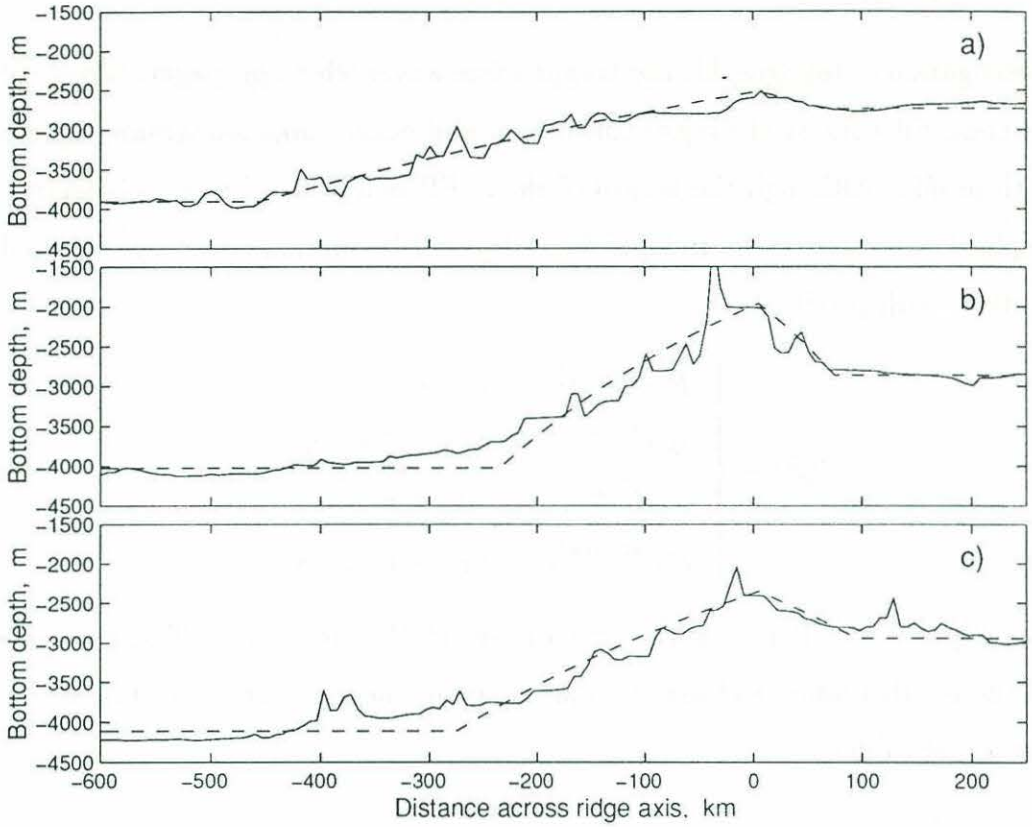

Figure 1-4: The topography of the Juan de Fuca Ridge along the three cross sections shown in Figure 1-1 (—-) fit by the simplified model topography (−−) defined by (1.2). The parameters for each are: a) $L_1 = 460$, $L_2 = 60$, $\alpha_1 = 0.0005$, $\alpha_2 = 0.0007$; b) $L_1 = 240$, $L_2 = 70$, $\alpha_1 = 0.0015$, $\alpha_2 = 0.0027$; and c) $L_1 = 280$, $L_2 = 90$, $\alpha_1 = 0.0010$, $\alpha_2 = 0.0013$.

the double-exponential depth profile described by (1.2). The model fits are shown in Figure 1-4. Although the actual topography is quite rugged, the model is a reasonable representation of the general topographic trends.

The existence and behaviour of ridge waves will be explored in the following chapters using the simple topographic approximation described above. Barotropic ridge waves in a nondivergent ocean will be discussed in Chapter 2. Divergence, however, becomes important at large wavelengths when the long-wave approximation is not used. Horizontal divergence is therefore added to the barotropic ridge wave problem in Chapter 3. The effects of stratification on the nondivergent barotropic

ridge waves are examined in Chapter 4. The models discussed in Chapters 2-4 will then be applied to the JdFR and the Iceland-Faeroe Ridge in Chapter 5 and the results compared to observations from the ridges.

Chapter 2

Nondivergent barotropic ridge waves

The exploration of ridge waves begins with a barotropic model that neglects divergence. Using this simple model with the depth profile described in the first chapter ensures that the problem will initially be tractable. The complicating effects of divergence and stratification are then added to this primary model and explored in the following chapters.

2.1 Governing equations

Following the methods of Mysak *et al.* (1979) for ocean trench waves, the unforced linearized shallow water equations on an f-plane are used. They are given by

$$u_t - fv = -g\eta_x, \tag{2.1}$$

$$v_t + fu = -g\eta_y, \tag{2.2}$$

$$(Hu)_x + (Hv)_y = -\eta_t, \tag{2.3}$$

where x and y are the horizontal rectangular co-ordinates, t is time, u and v are the velocity components in the x- and y-directions, η is the surface elevation, f is the Coriolis parameter, g is the gravity constant, and $H = H(x, y)$ is the depth of the bottom.

Scaling equations (2.1) - (2.3), as well as (1.2), by

$$(x, y) = \frac{1}{L}(x', y'), \quad (u, v) = \frac{1}{U}(u', v'),$$
$$H = \frac{1}{H_0}(H'), \quad t = ft', \quad \eta = \frac{g}{UfL}\eta',$$
$$(\alpha_1, \alpha_2) = L(\alpha_1', \alpha_2'), \quad (L_1, L_2) = L(L_1', L_2'),$$

where the primed variables are dimensional, produces the nondimensional equations

$$u_t - v = -\eta_x, \tag{2.4}$$

$$v_t + u = -\eta_y, \tag{2.5}$$

$$(Hu)_x + (Hv)_y = -\frac{1}{S}\eta_t, \tag{2.6}$$

where $S = \frac{gH_0}{f^2L^2}$, and the nondimensional depth profile

$$H(x) = \begin{cases} e^{(2\alpha_1 L_1)}, & -\infty < x \leq -L_1 \\ e^{(-2\alpha_1 x)}, & -L_1 \leq x \leq 0 \\ e^{(2\alpha_2 x)}, & 0 \leq x \leq L_2 \\ e^{(2\alpha_2 L_2)}. & L_2 \leq x < \infty \end{cases} \tag{2.7}$$

Divergence is initially neglected to keep the problem as simple as possible. This assumption is justified as $S^{-1} << 1$ for most mid-ocean ridges. The continuity equation (2.6) then becomes

$$(Hu)_x + (Hv)_y = 0, \tag{2.8}$$

and the velocity components can now be expressed in terms of a mass transport streamfunction $\Psi(x, y, t)$, such that

$$-\Psi_y = Hu, \quad \Psi_x = Hv. \tag{2.9}$$

Since the ridge topography is independent of y, Ψ is assumed to have the plane wave form

$$\Psi = \psi(x)e^{i(ly - \sigma t)},$$

where σ is the radian frequency and l is the wavenumber in the y-direction, so that $u, v, \eta \propto e^{i(ly-\sigma t)}$. The assumption that $l > 0$ can also be made, without loss of

generality. Differentiating (2.4) with respect to y, subtracting (2.5) differentiated with respect to x and using (2.9) then gives the vorticity equation

$$\left(\frac{\psi_x}{H}\right)_x - \left(\frac{l}{\sigma}\frac{H_x}{H^2} + \frac{l^2}{H}\right)\psi = 0. \tag{2.10}$$

2.2 Derivation of dispersion relation

In the regions away from the ridge where the bottom slope is zero, (2.10) becomes

$$\psi_{xx} - l^2\psi = 0. \tag{2.11}$$

Over the ridge described by (2.7), (2.10) becomes

$$\psi_{xx} + 2\alpha_1\psi_x + \left(\frac{2\alpha_1 l}{\sigma} - l^2\right)\psi = 0, \quad -L_1 \le x \le 0 \tag{2.12}$$

$$\psi_{xx} - 2\alpha_2\psi_x + \left(-\frac{2\alpha_2 l}{\sigma} - l^2\right)\psi = 0. \quad 0 \le x \le L_2 \tag{2.13}$$

Since the waves are assumed to be trapped to the topography, ψ must decay away from the ridge and the solution to (2.11) - (2.13) is

$$\psi(x) = \begin{cases} f_1 e^{l(x+L_1)}, & -\infty < x \le -L_1 \\ e^{-\alpha_1 x}(c_1\cos(\beta_1 x) + c_2\sin(\beta_1 x)), & -L_1 \le x \le 0 \\ e^{\alpha_2 x}(d_1\cos(\beta_2 x) + d_2\sin(\beta_2 x)), & 0 \le x \le L_2 \\ f_2 e^{-l(x-L_2)}, & L_2 \le x < \infty \end{cases} \tag{2.14}$$

where $\beta_1 = \left[\frac{2\alpha_1 l}{\sigma} - l^2 - \alpha_1^2\right]^{\frac{1}{2}}$ and $\beta_2 = \left[-\frac{2\alpha_2 l}{\sigma} - l^2 - \alpha_2^2\right]^{\frac{1}{2}}$.

At discontinuities in H_x, the normal transport, Hu, and the pressure must be continuous. These conditions imply the jump conditions

$$[\psi(x)] = 0 \quad \text{at} \quad x = -L_1, 0, L_2, \tag{2.15}$$

$$[\psi_x(x)] = 0 \quad \text{at} \quad x = -L_1, 0, L_2. \tag{2.16}$$

The above solution for ψ, (2.14), may then be matched at $x = -L_1$, 0, and L_2 to get

$$f_1 = e^{\alpha_1 L_1}(c_1\cos(\beta_1 L_1) - c_2\sin(\beta_1 L_1)), \tag{2.17}$$

$$c_1 = d_1, \tag{2.18}$$

$$f_2 = e^{\alpha_2 L_2}(d_1\cos(\beta_2 L_2) + d_2\sin(\beta_2 L_2)), \tag{2.19}$$

respectively.

Taking the derivative of (2.14) with respect to x and using (2.17) - (2.19) gives

$$\psi_x(x) = \begin{cases} le^{\alpha_1 L_1}(c_1\cos(\beta_1 L_1) - c_2\sin(\beta_1 L_1)e^{l(x+L_1)}, & -\infty < x \leq -L_1 \\ -\alpha_1 e^{-\alpha_1 x}(c_1\cos(\beta_1 x) + c_2\sin(\beta_1 x)) \\ \qquad -\beta_1 e^{-\alpha_1 x}(c_1\sin(\beta_1 x) - c_2\cos(\beta_1 x)), & -L_1 \leq x \leq 0 \\ \alpha_2 e^{\alpha_2 x}(c_1\cos(\beta_2 x) + d_2\sin(\beta_2 x)) \\ \qquad -\beta_2 e^{\alpha_2 x}(c_1\sin(\beta_2 x) - d_2\cos(\beta_2 x)), & 0 \leq x \leq L_2 \\ -le^{\alpha_2 L_2}(c_1\cos(\beta_2 L_2) + d_2\sin(\beta_2 L_2)e^{-l(x-L_2)}. & L_2 \leq x < \infty \end{cases} \tag{2.20}$$

Because $\psi_x(x)$ is also continuous in x, (2.20) may be matched at $x = -L_1$, 0, and L_2 to get

$$c_1(\alpha_1 + \alpha_2) - c_2(\beta_1) + d_2(\beta_2) = 0, \tag{2.21}$$

$$c_1((\alpha_1 + l)\cos(B_1) - \beta_1\sin(B_1)) - c_2((\alpha_1 + l)\sin(B_1) + \beta_1\cos(B_1)) = 0, \tag{2.22}$$

$$c_1((\alpha_2 + l)\cos(B_2) - \beta_2\sin(B_2)) + d_2((\alpha + l)\sin(B_2) + \beta_2\cos(B_2)) = 0, \tag{2.23}$$

respectively, where $B_1 = \beta_1 L_1$ and $B_2 = \beta_2 L_2$.

Setting the determinant of coefficients for equations (2.21) - (2.23) equal to zero produces the general dispersion relation

$$\tan(B_1) = \frac{-\beta_1(\alpha_2^2 + \beta_2^2 - l^2)\tan(B_2) + 2l\beta_1\beta_2}{\beta_2(\alpha_1^2 + \beta_1^2 - l^2) + [l(\beta_1^2 + \beta_2^2 + p^2) + \alpha_1(q_2) + \alpha_2(q_1)]\tan(B_2)}, \tag{2.24}$$

where $p = \alpha_1 + \alpha_2$, $q_1 = (\alpha_1^2 + \beta_1^2 + l^2)$, and $q_2 = (\alpha_2^2 + \beta_2^2 + l^2)$.

Note that when $L_2 \to 0$, (2.24) becomes

$$\tan(\beta_1 L_1) = \frac{2l\beta_1}{(\alpha_1^2 + \beta_1^2 - l^2)}. \tag{2.25}$$

This agrees with the isolated shelf wave dispersion relation derived by Buchwald and Adams (1968). Their model was of a single exponential slope separating two flat regions, which is equivalent to the model ridge topography with $L_2 = 0$.

So that there will exist an infinite number of positive real roots for the western slope of the ridge, β_{1_n} $(n = 0, 1, 2, \ldots)$ for fixed l and σ, σ must fall in the range of

$$0 < \sigma < \frac{2\alpha_1 l}{\alpha_1^2 + l^2}. \tag{2.26}$$

Using the assumption $l > 0$, these waves are found to propagate northward with shallow water on their right.

Equivalently, so that there will exist an infinite number of positive real roots for the waves on the eastern side of the ridge, $\beta_{2_n}(n = 0, 1, 2, ...)$ for fixed l and σ, σ must fall in the range of

$$\frac{-2\alpha_2 l}{\alpha_2^2 + l^2} < \sigma < 0. \tag{2.27}$$

These waves move toward the south, also with the shallow water on their right. The ridge supports a set of waves on each side that travel in opposite directions.

2.3 Dispersion curves

Because real solutions are sought, the waves on the eastern and western sides of the ridge must be treated separately. On the western slope, $\sigma > 0$, β_1 is positive and real, and β_2 is imaginary. Thus, let $M = i\beta_2$ and (2.24) becomes

$$\tan(B_1) = \frac{-\beta_1(\alpha_2^2 - M^2 - l^2)\tanh(ML_2) + 2l\beta_1 M}{M(\alpha_1^2 + \beta_1^2 - l^2) + [l(\beta_1^2 - M^2 + p^2) + \alpha_1 q_2^* + \alpha_2 q_1]\tanh(ML_2)}, \tag{2.28}$$

where $M = i\beta_2 = \left[\frac{2\alpha_2 l}{\sigma} + l^2 + a_2^2\right]^{\frac{1}{2}}$ and $q_2^* = (\alpha_2^2 - M^2 + l^2)$.

It must be recognized, however, that for $n = 0$ in the limit of $\beta_1 \to 0$

$$L_1^2\{M(\alpha_1^2 - l^2) + [l(-M^2 + p^2 + \alpha_1 q_2^* + \alpha_2(\alpha_1^2 + l^2)]\tanh(ML_2)\}$$
$$= -L_1[q_2^*\tanh(ML_2) - 2Ml]. \tag{2.29}$$

From this expression it can be shown that a minimum value of $l = l_1$ occurs for real β_1. The lowest mode, therefore, does not have real solutions over the full range of l because β_1 is imaginary for $l < l_1$.

On the eastern slope, $\sigma < 0$, β_2 is positive and real, and β_1 is imaginary. Thus let $N = i\beta_1$ and (2.24) becomes

$$\tan(B_2) = \frac{-\beta_2(\alpha_1^2 - N^2 - l^2)\tanh(NL_1) + 2l\beta_2 N}{N(\alpha_2^2 + \beta_2^2 - l^2) + [l(\beta_2^2 - N^2 + p^2) + \alpha_1 q_2 + \alpha_2 q_1^*]\tanh(NL_1)}, \tag{2.30}$$

where $N = i\beta_1 = \left[\frac{-2\alpha_1 l}{\sigma} + l^2 + a_1^2\right]^{\frac{1}{2}}$ and $q_1^* = (\alpha_1^2 - N^2 + l^2)$.

It can also be verified that for $n = 0$ a minimum value of $l = l_2$ occurs for real β_2 as in the case of the western slope waves. The lowest mode does not have real solutions over the full range of l because β_2 is imaginary for $l < l_2$.

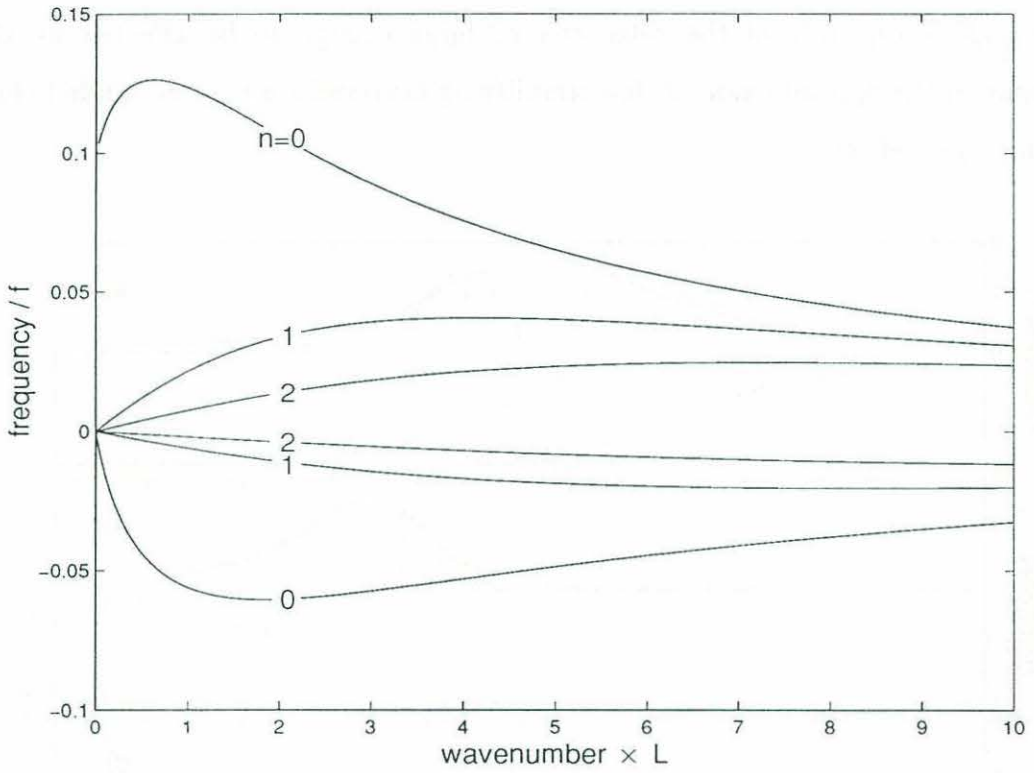

Figure 2-1: The ridge wave dispersion curves of the first three modes for the ridge described by $L_1 = 1$, $L_2 = 0.5$, $\alpha_1 = 0.2$, and $\alpha_2 = 0.2$.

The dispersion relations (2.28) and (2.30) can now be solved over a range of l to get the dispersion curves. The first three modes of both the western and eastern slope waves for a generic ridge are shown in Figure 2-1. For small l the group and phase velocities of the waves are in the same direction, but for large l the group velocity is in the opposite direction. There is a point then in the transition between these two regimes in l where the slope of the curve is zero and the group velocity vanishes. Energy might therefore tend to accumulate along the ridge at this frequency and wavenumber. The point at which the group velocity of the lowest mode goes to zero (the ZGV) will be sought out as it corresponds to the frequency and wavenumber at which peaks in energy may be observed. It also represents the maximum frequency

at which these waves can occur.

The ridge wave eigenfunctions, $\psi(x)$, for the first three modes of both the western and eastern slope ridge waves over a generic ridge are shown in Figure 2-2. Although there is rapid decay away from the slope that supports each set of modes, the waves travelling along one side of the ridge can be large enough to be affected by the topography of the opposite side. A few simplifying assumptions may be made before examining these effects.

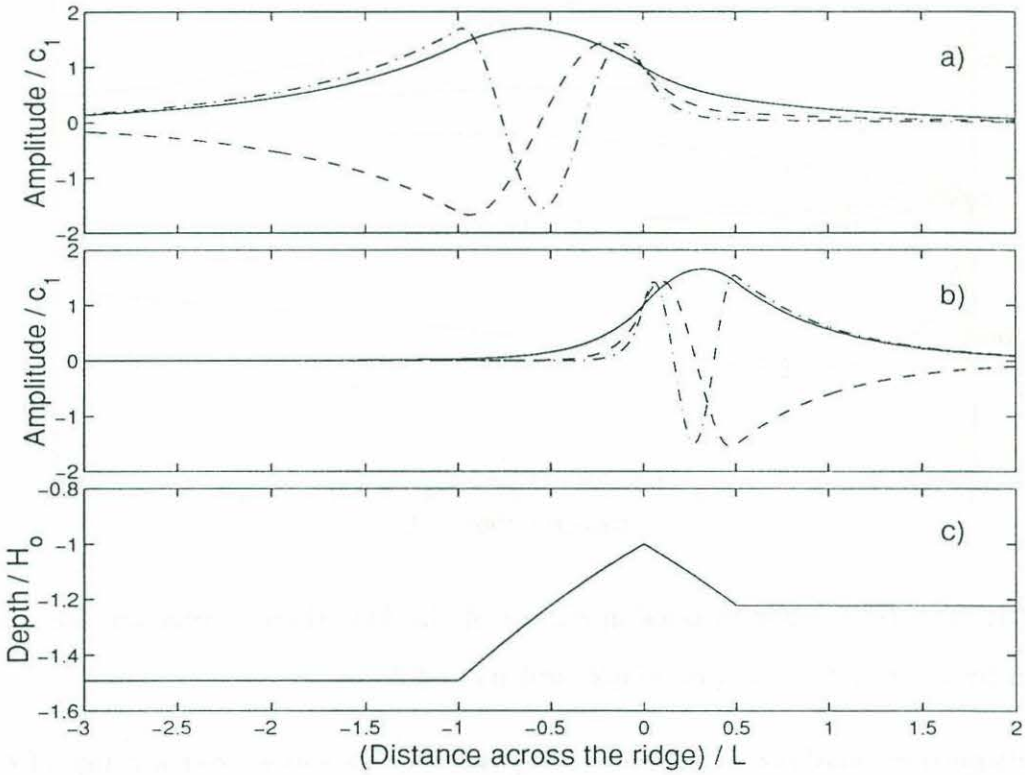

Figure 2-2: The a) western slope and b) eastern slope eigenfunctions, $\Psi(x)$, for the first three ridge wave modes ($l = 1.0$) over the ridge shown in c) where $L_1 = 1$, $L_2 = 0.5$, $\alpha_1 = 0.2$, and $\alpha_2 = 0.2$.

Because the orientation of the ridge does not affect the governing equations, the assumption that $L_1' > L_2'$ can be made without loss of generality. The length scale, L, will then be equivalent to L_1' and the behaviour of the ridge waves over various depth profiles may be explored.

The ridge waves are first explored while keeping the shape of the eastern side of the

ridge constant. Since $L_1 \equiv 1$ only α_1 is varied on the western side. Figure 2-3 shows the effect of varying α_1 on the lowest mode of the ridge waves. As the western side of the ridge becomes steeper, the phase velocities of the waves it supports become faster due to an increase in the frequencies over the entire range of l. The wavenumber of the ZGV also becomes smaller. The frequencies of the eastern slope waves decrease as the influence of the western slope increases.

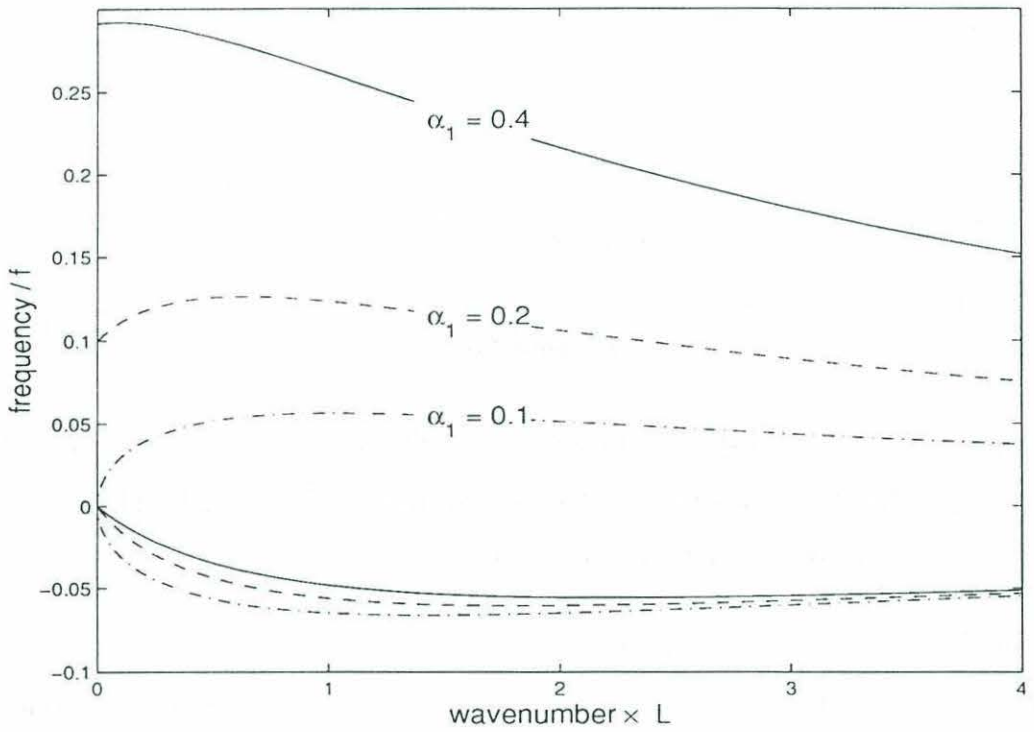

Figure 2-3: The ridge wave dispersion curves of the first mode for the ridges described by $L_1 = 1$, $L_2 = 0.5$, $\alpha_2 = 0.2$ and $\alpha_1 = 0.1,\ 0.2,\ 0.4$. The linetypes for $\sigma < 0$ correspond to the linetypes for $\sigma > 0$.

Changing the parameters on the eastern side of the ridge also affects the waves on the western side. Note that in the limit $L_2 \to 0$, the topography becomes an isolated shelf. Over an isolated shelf, the lowest mode approaches a non-zero finite number as $l \to 0$ due to the neglection of divergence in the continuity equation. (Buchwald and Adams, 1968) The group and phase velocities are always in opposite directions and there is no ZGV for the lowest mode over an isolated shelf when divergence is

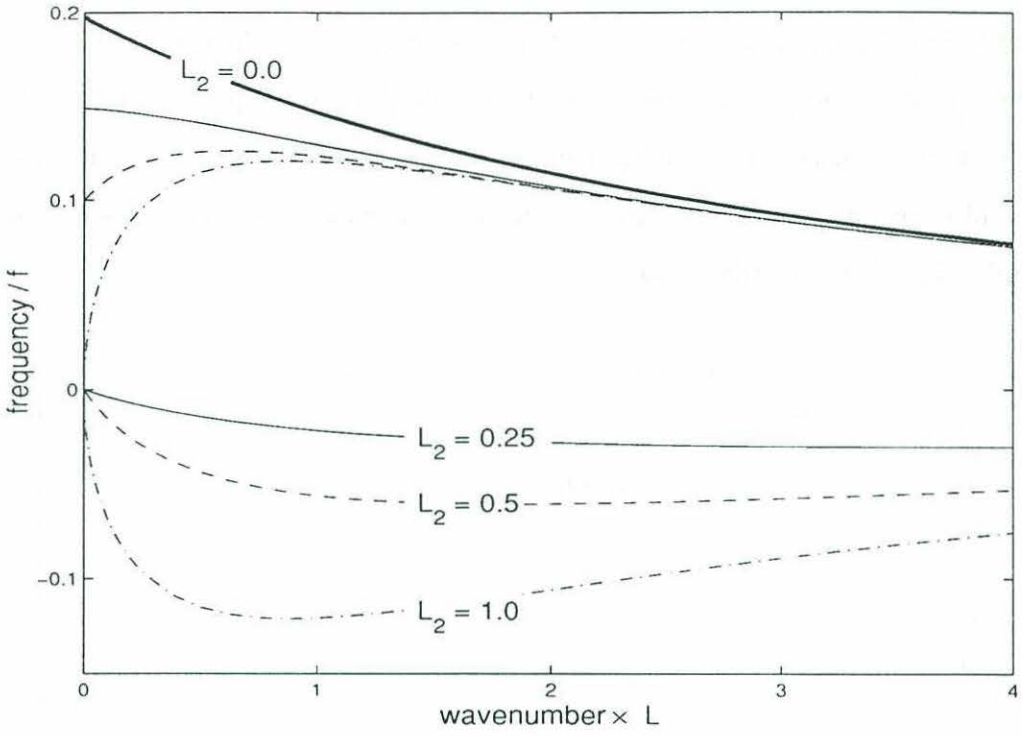

Figure 2-4: The ridge wave dispersion curves of the first mode for the ridges described by $L_1 = 1$, $\alpha_1 = 0.2$, $\alpha_2 = 0.2$ and $L_2 = 0$ (isolated shelf), 0.25, 0.5, 1.0. The linetypes for $\sigma > 0$ correspond to the linetypes for $\sigma < 0$.

not included in the continuity equation.

As can be seen in Figure 2-4, increasing L_2 causes the lowest mode to develop a ZGV that decreases in frequency space and increases in wavenumber space for the western slope waves and the reverse for the eastern slope waves. For small wavelengths the two sides of the ridge become 'separated' and the opposite side of the ridge is not felt. Consequently, the western slope dispersion curves approach the isolated shelf dispersion curve at large l. The effect of increasing the width of the eastern side, therefore, is an decrease in the phase speed of the waves on the western side at moderate to large wavelengths and an increase in the phase speed of the waves on the eastern side.

Similarly, as $\alpha_2 \to 0$ the ridge topography begins to look like an isolated shelf. As the ridge moves away from this limit (α_2 increases) the lowest mode on the western

slope develops a ZGV that decreases in frequency space and increases in wavenumber space, as shown in Figure 2-5. The effect of increasing the slope of the eastern side is also to slow the phase speed of the western slope waves for moderate to large wavelengths and accelerate the phase speed of the eastern slope waves.

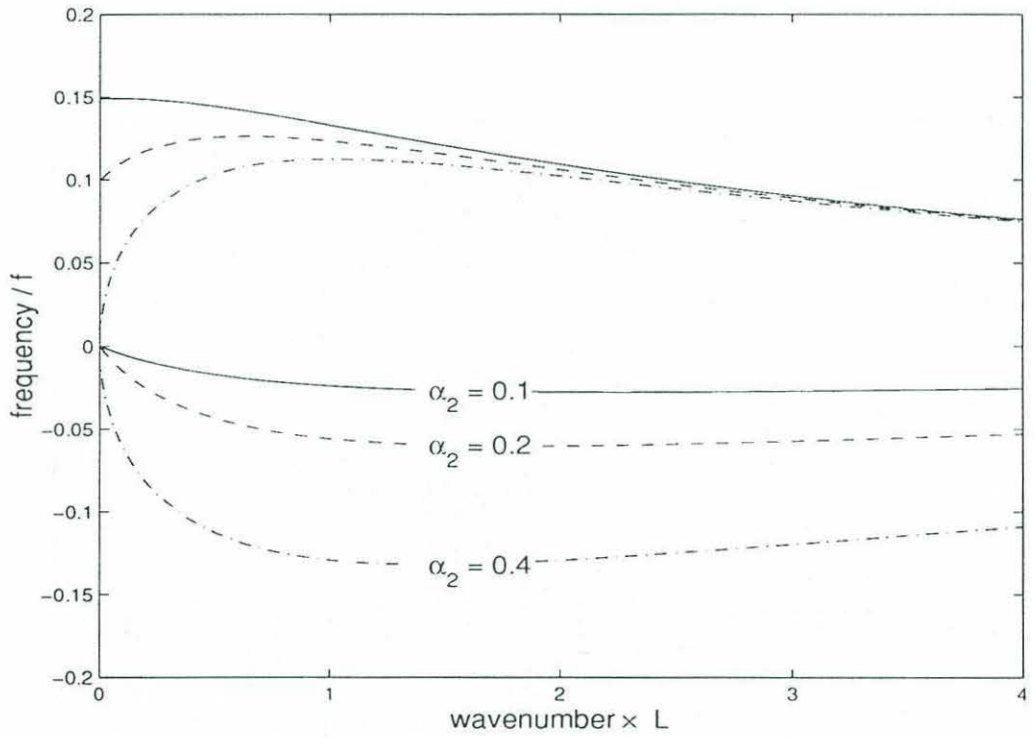

Figure 2-5: The ridge wave dispersion curves of the first mode for the ridges described by $L_1 = 1$, $L_2 = 0.5$, $\alpha_1 = 0.2$ and $\alpha_1 = 0.1$, 0.2, 0.4. The linetypes for $\sigma > 0$ correspond to the linetypes for $\sigma < 0$.

It is apparent that a ZGV will not be found for the lowest mode of some ridges if divergence is neglected. As the ridges approach the limit of an isolated shelf, the lowest mode shows unique behaviour in that the group and phase velocities are always in opposite directions. The higher modes do not show the same trend. Divergence will be added in the next chapter to rectify this situation.

2.4 Velocity fields

The velocity fields across the ridge may be found by substituting the final form of (2.14) for a given l into (2.9). Figures 2-6 and 2-7 show the velocity fields for the waves supported on the western and eastern slopes of a generic ridge at their respective ZGV frequencies.

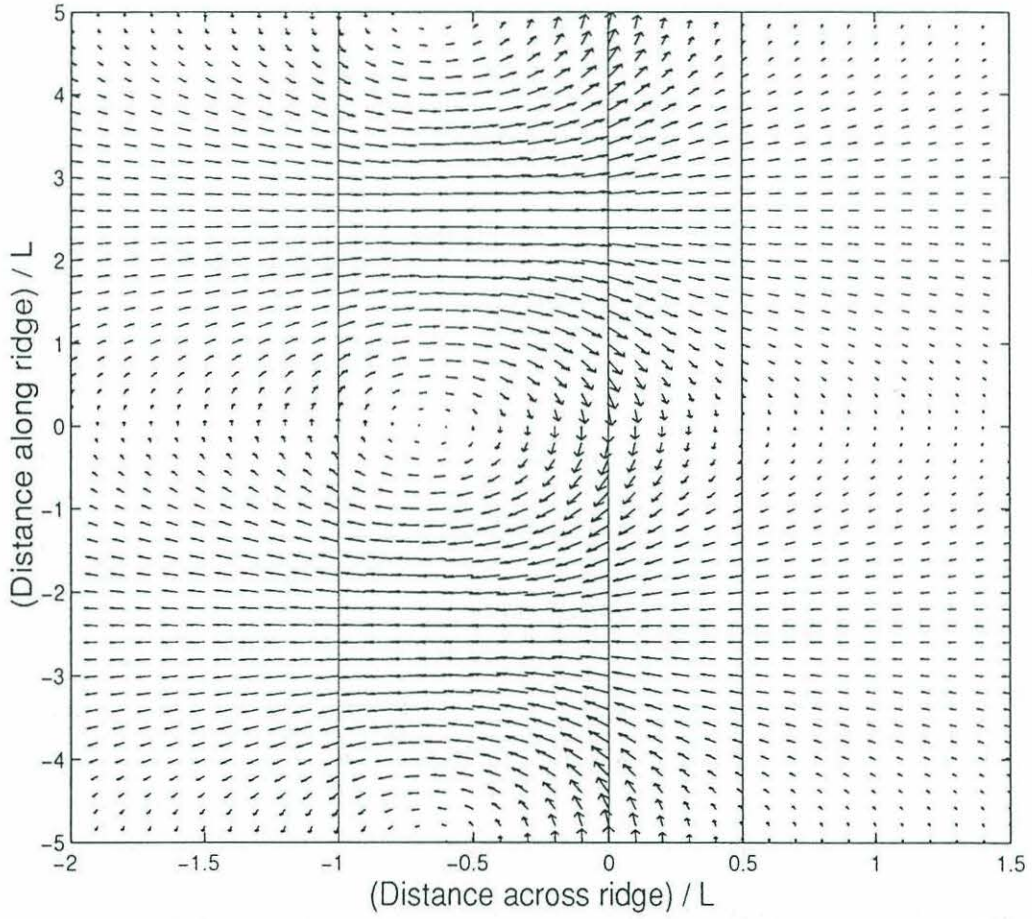

Figure 2-6: The velocity field due to the lowest mode of the western slope ridge wave at $t = 0$. ($k = 0.625$, $\sigma = 0.126$) The ridge is described by $L_1 = 1.0$, $L_2 = 0.5$, $\alpha_1 = 0.2$, $\alpha_2 = 0.2$ and is shown by the solid lines.

As a ridge wave propagates by a moored velocity sensor, the velocity vectors seen by the mooring will rotate in the sense of the passing velocity field. As shown in Figure 2-8, the motion is nearly circular away from the ridge, but becomes elliptical

over the ridge flanks. In addition, the velocity ellipses are anticyclonic near the crest of the ridge and cyclonic away from the ridge crest on the side of the ridge that is supporting the wave for both sets of ridge waves. This corresponds to the primarily anticyclonic subinertial signal seen in the power spectra of velocities over the ridge axis in Figure 1-2.

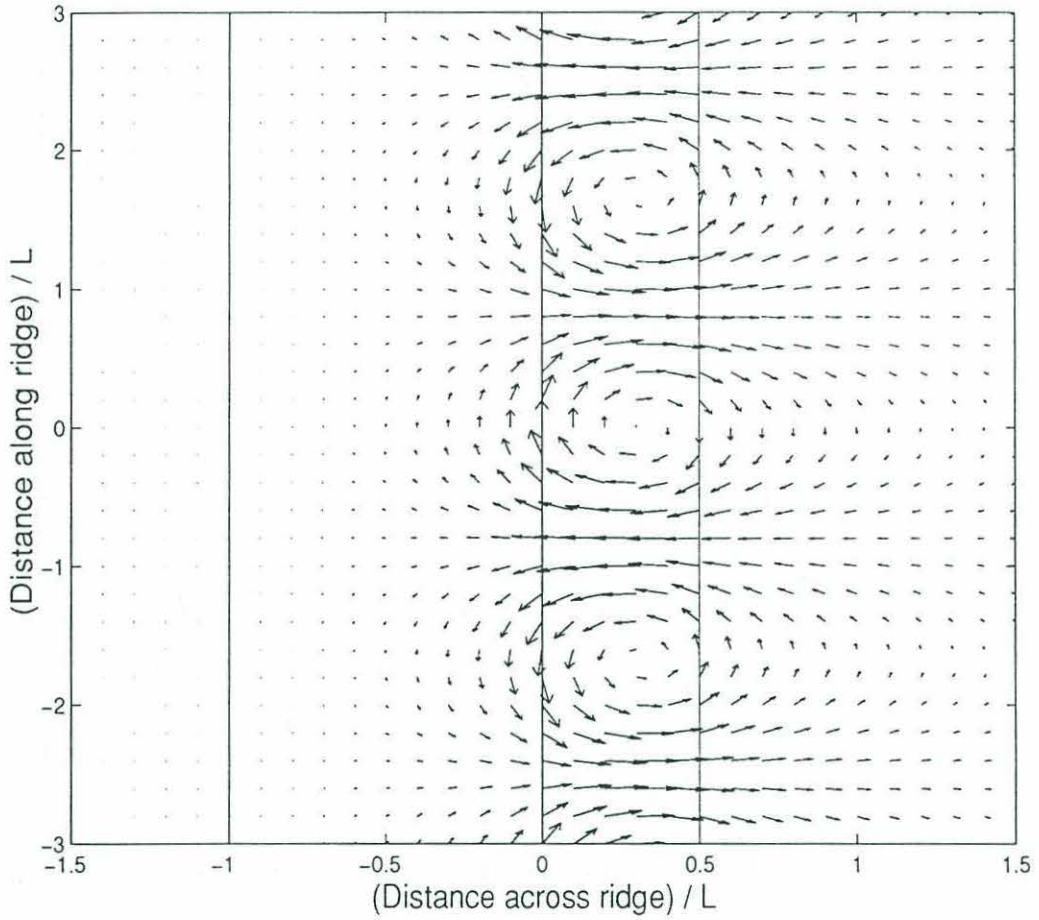

Figure 2-7: The velocity field due to the lowest mode of the eastern slope ridge wave at $t = 0$. ($k = 1.875$, $\sigma = -0.060$) The ridge is described by $L_1 = 1.0$, $L_2 = 0.5$, $\alpha_1 = 0.2$, $\alpha_2 = 0.2$ and is shown by the solid lines.

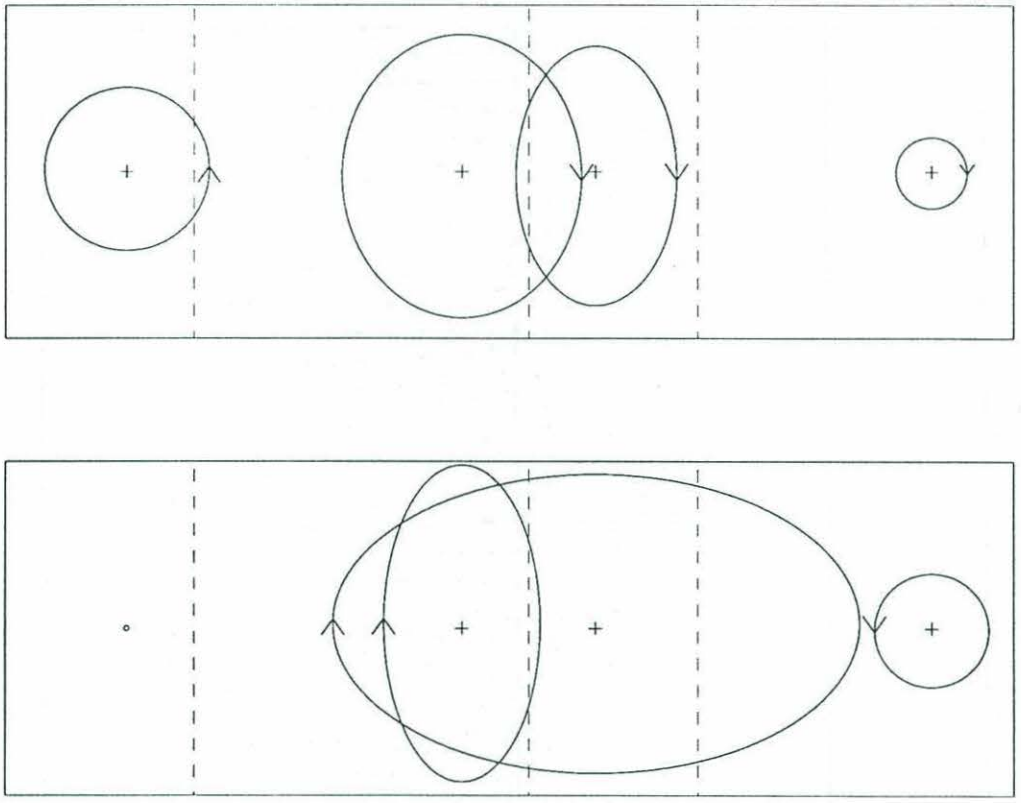

Figure 2-8: The velocity ellipses due to the lowest mode of the western slope ridge waves. ($k = 0.625$, $\sigma = 0.126$) The velocity ellipses due to the lowest mode of the eastern slope ridge waves. ($k = 1.875$, $\sigma = -0.060$) The ridge is described by $L_1 = 1.0$, $L_2 = 0.5$, $\alpha_1 = 0.2$, $\alpha_2 = 0.2$ and is shown by the dashed lines.

Chapter 3

Divergent barotropic ridge waves

Because of the potential problems for the lowest mode at small l in the nondivergent barotropic ridge model dicussed in the previous chapter, a divergent model is now examined. Including divergence will lower the frequency of the longest waves since the raising of the free surface due to an upslope motion opposes spin-down. (Rhines, 1969)

3.1 Governing equations

Divergence is added back into the previous model by using the full continuity equation (2.6). Equations (2.4) - (2.6) may now be solved for an equation in η,

$$(H\eta_x)_x - \left(\frac{1}{S}(1-\sigma^2) + l^2 H + \frac{lH_x}{\sigma}\right)\eta = 0. \tag{3.1}$$

In the flat region to the west of the ridge, where the depth is $H_W = e^{2\alpha_1 L_1}$, (3.1) becomes

$$\eta_{xx} - k_1^2\eta = 0, \tag{3.2}$$

where

$$k_1^2 = \frac{1}{H_W}\left(\frac{1}{S}(1-\sigma^2) + l^2 H_W\right).$$

In the flat region to the east of the ridge, where the depth is $H_E = e^{2\alpha_2 L_2}$, (3.1) becomes

$$\eta_{xx} - k_2^2 \eta = 0, \tag{3.3}$$

where

$$k_2^2 = \frac{1}{H_E}\left(\frac{1}{S}(1-\sigma^2) + l^2 H_E\right).$$

Again, the solutions are in the form of waves trapped to the ridge, so

$$\eta(x) = \begin{cases} g_1 e^{k_1(x+L_1)}, & -\infty < x \leq -L_1 \\ g_2 e^{-k_2(x-L_2)}. & L_2 \leq x < \infty \end{cases} \tag{3.4}$$

The derivative of (3.4) with respect to x is then

$$\eta_x(x) = \begin{cases} k_1 g_1 e^{k_1(x+L_1)}, & -\infty < x \leq -L_1 \\ -k_2 g_2 e^{-k_2(x-L_2)}. & L_2 \leq x < \infty \end{cases} \tag{3.5}$$

To solve (3.1) over the ridge itself, the second-order equation is broken down into two first-order equations by assigning the values

$$y_1 = \eta, \tag{3.6}$$

$$y_2 = \eta_x. \tag{3.7}$$

In addition,

$$y_3 = H(x) \tag{3.8}$$

is also defined so that over the western slope of the ridge ($-L_1 < x < 0$) the x-derivatives of (3.6) - (3.8) become

$$y_1' = y_2, \tag{3.9}$$

$$y_2' = \left(\frac{1-\sigma^2}{S y_3} + l^2 - \frac{2\alpha_1 l}{\sigma}\right) y_1 + 2\alpha_1 y_2, \tag{3.10}$$

$$y_3' = -2\alpha_1 y_3, \tag{3.11}$$

and over the eastern slope of the ridge ($0 < x < L_2$) the x-derivatives of (3.6) - (3.8) become

$$y_1' = y_2, \tag{3.12}$$

$$y_2' = \left(\frac{1-\sigma^2}{Sy_3} + l^2 + \frac{2\alpha_2 l}{\sigma}\right) y_1 - 2\alpha_2 y_2, \tag{3.13}$$

$$y_3' = 2\alpha_2 y_3. \tag{3.14}$$

Following the method described in Stoer and Bulirsch (1991), this eigenvalue problem (σ is the eigenvalue) can be reduced to a boundary-value problem by adding

$$y_4 = \sigma \tag{3.15}$$

to the above set of equations so that

$$y_4' = 0. \tag{3.16}$$

Because pressure and velocity are continuous across the domain, the boundary conditions imposed are the jump conditions

$$[y_1] = [\eta] = 0, \tag{3.17}$$

$$[y_2] = [\eta_x] = 0, \tag{3.18}$$

at $x = -L_1, 0, L_2$ so that the solutions for η and η_x are continuous in x.

To get the initial conditions for (3.9) and (3.10), (3.4) and (3.5) are solved at $x = -L_1$ using $g_1 = 1$. The initial value for (3.11) is just H_W. Equations (3.9) - (3.14) and (3.16) are then solved over the range $-L_1 \leq x \leq L_2$ with the above initial conditions and a range of values for $y_4 = \sigma$. The constant g_2 is found by determing the value of $y_1(x = L_2)$ from shooting across the ridge and setting it equal to (3.4) at $x = L_2$ so that

$$g_2 = y_1(x = L_2). \tag{3.19}$$

The value of σ that satisfies (3.6) - (3.18) is determined by solving (3.19) for g_2 over a range of σ and finding the one that will also satisfy the other condition at $x = L_2$,

$$y_2(x = L_2) = \eta_{1_x}(x = L_2) = -k_2 g_2(\sigma). \tag{3.20}$$

3.2 Dispersion curves

The divergent dispersion curves that result from the above calculations for a generic ridge are shown in Figure 3-1 as well as the corresponding nondivergent curves. The curves are indistinguishable except for the behaviour of the lowest mode at small l. Because of the inclusion of divergence, $\sigma \to 0$ as $l \to 0$. The higher modes are not affected. Note that including divergence lowers the frequecy of the ZGV as well as increasing the wavenumber, thus lowering the phase velocity of the energy trapped waves.

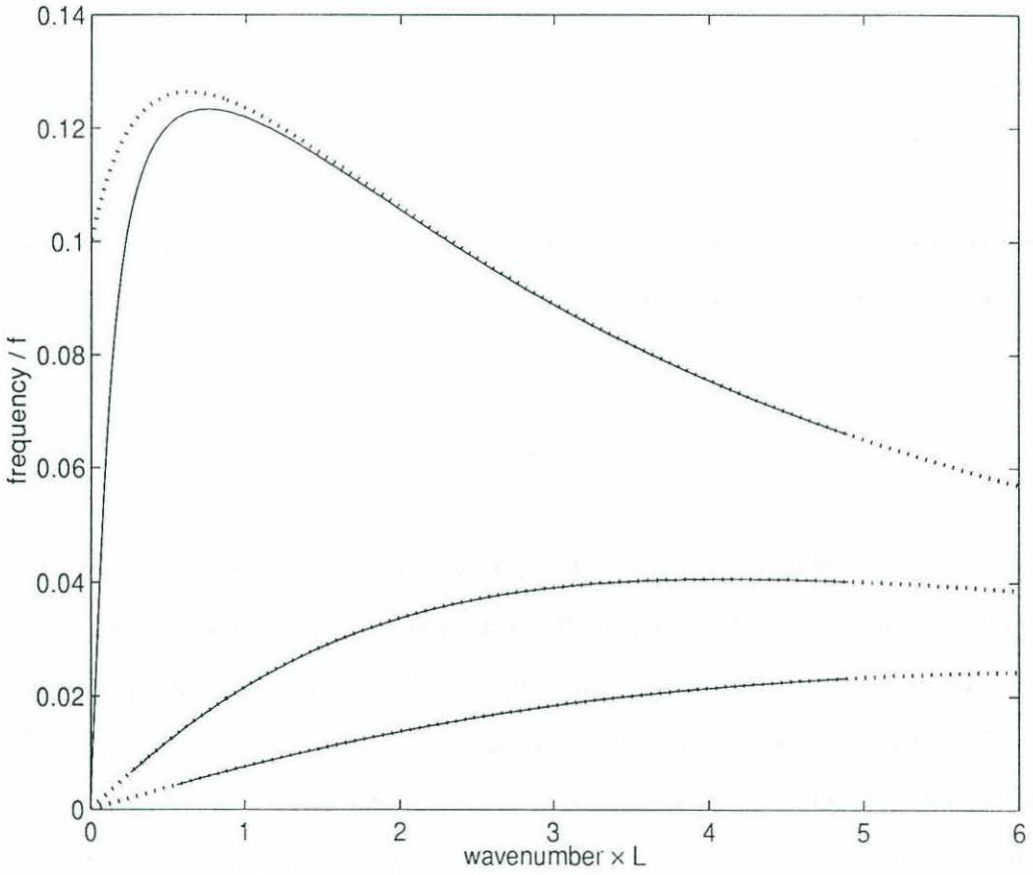

Figure 3-1: The ridge wave dispersion curves of the three lowest modes with divergence (—) and without divergence ($\cdots$) over the ridge described by $L_1 = 1$, $L_2 = 0.5$, $\alpha_1 = 0.2$, and $\alpha_2 = 0.2$.

As shown in Figure 3-2, the lowest mode for an isolated shelf topography in a divergent ocean is now well behaved at small l and is again the limit for the ridge

waves as $L_2 \to 0$. With the increasing influence of the topography on the opposite slope as L_2 increases, however, the phase velocities of the western slope waves are once again decreased.

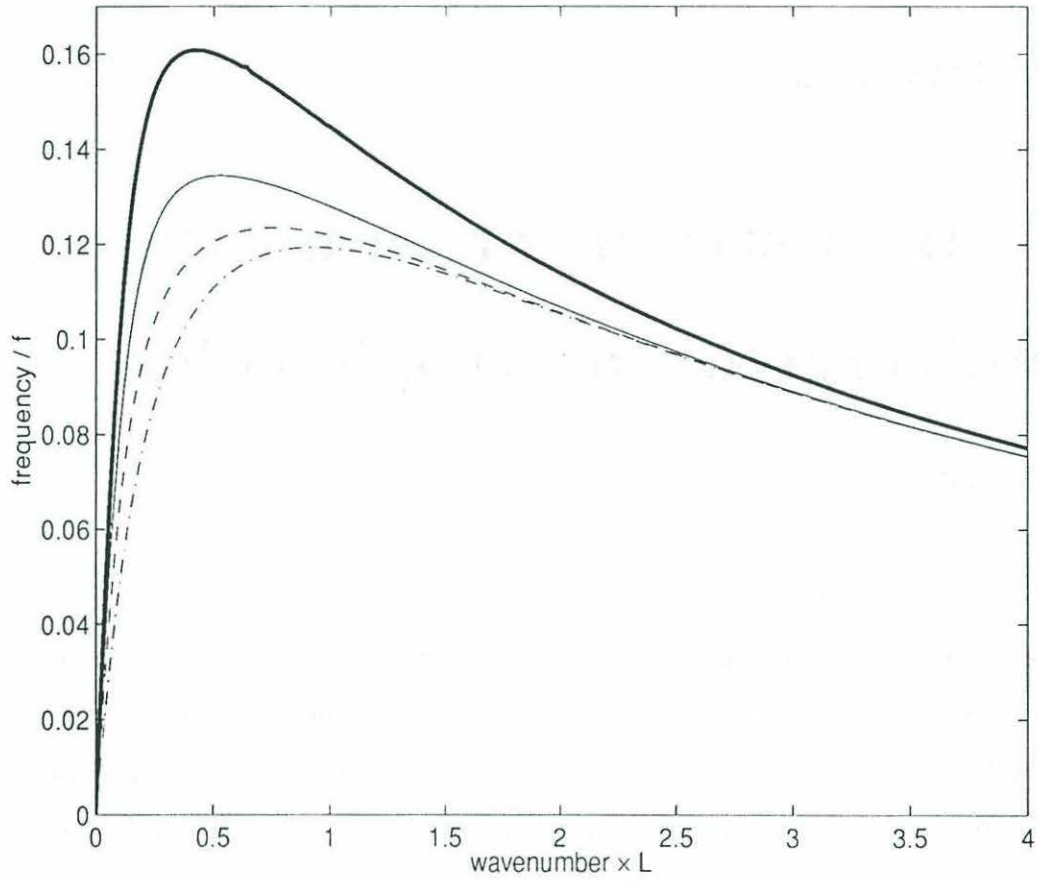

Figure 3-2: The divergent ridge wave dispersion curves of the first mode for the ridges described by $L_1 = 1$, $\alpha_1 = 0.2$, $\alpha_2 = 0.2$ and $L_2 = 0$ (━━), 0.25 (—), 0.5 (– –), 1.0 (· – ·–).

Chapter 4

Effects of stratification on the nondivergent barotropic ridge waves

In addition to topographic variations, stratification can also play a role in trapping waves. Allen (1975) determined that the effects of topography and stratification on coastal trapped waves over a continental shelf produce both a baroclinic and a barotropic mode that are coupled at the lowest order. The motion is primarily confined to the bottom layer of a two-layer ocean and is therefore bottom-trapped. It is then reasonable to assume that a similar coupling occurs over mid-ocean ridges. The baroclinic solution is not determined here, but the influences of stratification on the barotropic solution are examined by a perturbation procedure.

A two-layer system is now defined so that the effects of stratification on the problem of waves trapped to ridges may be examined. The total depth is represented by

$$H_T(x) = H_1 + \begin{cases} H_0 e^{(2\alpha_1 L_1)}, & -\infty < x \leq -L_1 \\ H_0 e^{(-2\alpha_1 x)}, & -L_1 \leq x \leq 0 \\ H_0 e^{(2\alpha_2 x)}, & 0 \leq x \leq L_2 \\ H_0 e^{(2\alpha_2 L_2)}, & L_2 \leq x < \infty, \end{cases} \tag{4.1}$$

where H_1 is the undisturbed constant thickness of the upper layer.

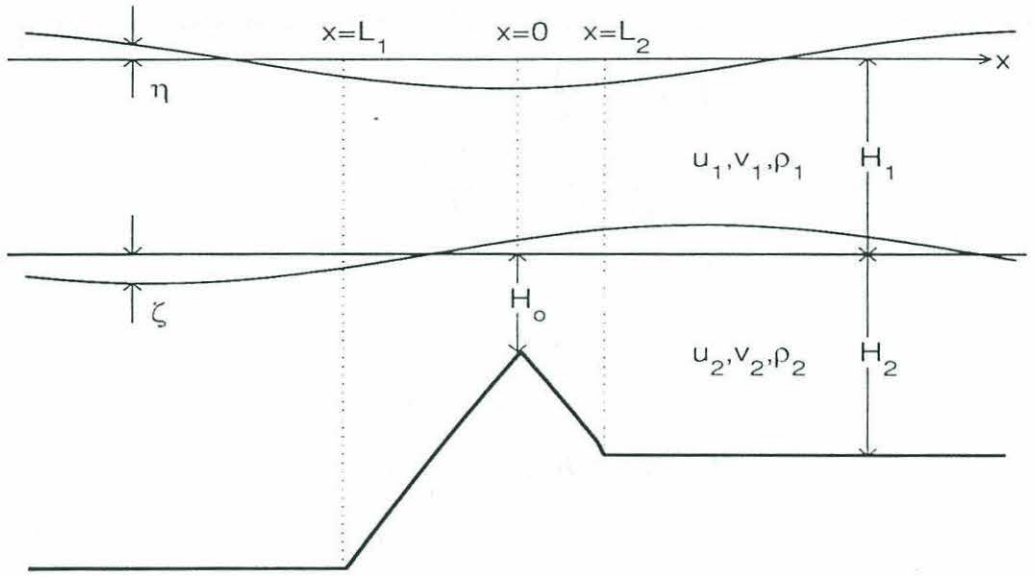

Figure 4-1: The two-layer model configuration used to study the effects of stratification on the barotropic ridge waves.

4.1 Governing equations

The appropriate equations for a nondivergent two-layer ocean are

$$u_{1_t} - fv_1 = -g\eta_x, \tag{4.2}$$

$$v_{1_t} + fu_1 = -g\eta_y, \tag{4.3}$$

$$H_1(u_{1_x} + v_{1_y}) = \zeta_t, \tag{4.4}$$

$$u_{2_t} - fv_2 = -g\eta_x - g'\zeta_x, \tag{4.5}$$

$$v_{2_t} + fu_2 = -g\eta_y - g'\zeta_y, \tag{4.6}$$

$$(H_2u_2)_x + (H_2v_2)_y = -\zeta_t, \tag{4.7}$$

where u_1 and v_1 are the velocity components in the upper layer, u_2 and v_2 are the velocity components in the lower layer, H_1 is the undisturbed thickness of the upper layer, $H_2(x)$ is the undisturbed thickness of the lower layer, η is the surface height, ζ is the height of the interface between the two layers, and $g' = \frac{\Delta\rho}{\rho_2}g$, where $\Delta\rho$ is the density difference between the two layers $(\rho_2 - \rho_1)$ so that $\frac{\Delta\rho}{\rho_2} << 1$. The parameters for the model are shown in Figure 4-1.

In addition to the scaling factors used for the barotropic ridge waves in Chapter 2,

$$(H_1, H_2) = \frac{1}{H_*}(H_1', H_2'),$$
$$\zeta = \frac{\Delta\rho g}{\rho_2 U f L}\zeta' = \frac{g\prime}{U f L}\zeta',$$

are also used to get the non-dimensional equations

$$u_{1_t} - v_1 = -\eta_x, \tag{4.8}$$
$$v_{1_t} + u_1 = -\eta_y, \tag{4.9}$$
$$(H_1 u_1)_x + (H_1 v_1)_y = \frac{1}{B_u}\zeta_t, \tag{4.10}$$
$$u_{2_t} - v_2 = -\eta_x - \zeta_x, \tag{4.11}$$
$$v_{2_t} + u_2 = -\eta_y - \zeta_y, \tag{4.12}$$
$$(H_2 u_2)_x + (H_2 v_2)_y = -\frac{1}{B_u}\zeta_t, \tag{4.13}$$

where B_u is defined as the Burger number

$$B_u = \frac{\frac{g\Delta\rho}{\rho_2 H_*}H_*^2}{f^2 L^2} << 1$$

Free wave solutions are sought, so let

$$\zeta = \zeta_*(x)e^{i(ly-\sigma t)}, \tag{4.14}$$
$$\eta = \eta_*(x)e^{i(ly-\sigma t)}. \tag{4.15}$$

Solving for u_1, u_2, v_1, and v_2 in terms of η and ζ from equations (4.8), (4.9), (4.11), and (4.12) then gives

$$u_1 = -\frac{1}{(1-\sigma^2)}(\eta_{xt} + \eta_y), \tag{4.16}$$
$$v_1 = \frac{1}{(1-\sigma^2)}(\eta_x - \eta_{yt}), \tag{4.17}$$
$$u_2 = -\frac{1}{(1-\sigma^2)}(\eta_{xt} + \eta_y + \zeta_x + \zeta_y), \tag{4.18}$$
$$v_2 = \frac{1}{(1-\sigma^2)}(\eta_x - \eta_{yt} + \zeta_x - \zeta_{yt}). \tag{4.19}$$

By adding (4.10) and (4.13) together it is apparent that a mass transport stream function, $\Psi(x, y, t)$, may be defined such that

$$\Psi_x = (H_1 v_1 + H_2 v_2), \quad \Psi_y = -(H_1 u_1 + H_2 u_2). \tag{4.20}$$

Substituting (4.16) - (4.19) into (4.20) produces values of u_1, u_2, v_1 and v_2 in terms of Ψ and ζ only:

$$u_1 = -\frac{\Psi_y}{H_T} + \frac{H_2}{H_T(1-\sigma^2)}(\zeta_{xt} + \zeta_y), \tag{4.21}$$

$$v_1 = \frac{\Psi_x}{H_T} - \frac{H_2}{H_T(1-\sigma^2)}(\zeta_x - \zeta_{yt}), \tag{4.22}$$

$$u_2 = -\frac{\Psi_y}{H_T} - \frac{H_1}{H_T(1-\sigma^2)}(\zeta_{xt} + \zeta_y), \tag{4.23}$$

$$v_2 = \frac{\Psi_y}{H_T} - \frac{H_1}{H_T(1-\sigma^2)}(\zeta_x - \zeta_{yt}). \tag{4.24}$$

Differentiating (4.8) by y, subtracting (4.9) differentiated by x, and substituting the result into (4.10) gives

$$(u_{1_y} - v_{1_x})_t = \frac{1}{H_1 B_u}\zeta_t. \tag{4.25}$$

Similarly, in the lower layer, equations (4.11) - (4.13) become

$$(u_{2_y} - v_{2_x})_t = -\frac{H_{2_x}}{H_2}u_2 - \frac{1}{H_2 B_u}\zeta_t. \tag{4.26}$$

One of the desired equations can be produced by adding $H_1 \times$(4.25) and $H_2 \times$(4.26) and then using (4.20) to get

$$\nabla_H^2 \Psi_t = H_{2_x} v_{2_t} + H_{2_x} u_2. \tag{4.27}$$

A "barotopic" mode equation can then be written in terms of Ψ and ζ only by substituting (4.21) - (4.24) into (4.27) to get

$$\nabla_H^2 \Psi_t = \frac{H_{T_x}}{H_T}(\Psi_{xt} - \Psi_y - H_1 \zeta_y), \tag{4.28}$$

where Ψ represents the barotropic component of the motion, ζ represents the baroclinic component of the motion, and the fact that $H_{T_x} = H_{2_x}$ has been used.

Similarly, a "baroclinic" mode equation can be derived by subtracting (4.25) from (4.26) and then using (4.20) to get

$$(u_{2_y} - v_{2_x})_t + \frac{H_{2_x}}{H_2}u_2 + \frac{1}{H_2 B_u}\zeta_t - (u_{1_y} - v_{1_x})_t + \frac{1}{H_1 B_u}\zeta_t = 0. \tag{4.29}$$

Substituting (4.21) - (4.24) into (4.29) then gives

$$\nabla_H^2 \zeta_t + \frac{H_1}{H_2}\frac{H_{T_x}}{H_T}(\zeta_{xx} + \zeta_y) - \frac{(1-\sigma^2)}{\bar{H}B_u}\zeta_t = -\frac{H_{T_x}(1-\sigma^2)}{H_2 H_T}\Psi_y, \tag{4.30}$$

where $\bar{H} = \frac{H_1 H_2}{H_T}$. Note that the coupling between (4.28) and (4.30) is dependent on the presence of a non-uniform bottom topography.

4.2 Perturbation solutions

Because of the complex nature of the coupled barotropic and baroclinic modes found in the previous section, analytical solutions are impractical. Instead, following the methods used by Allen (1975) to study coastal trapped waves in a stratified ocean, perturbation methods will be used to examine the modification of the barotropic ridge waves by the baroclinic component of motion.

Since the solutions were assumed to be of the form $e^{i(ly-\sigma t)}$, the coupled second order equations, (4.28) and (4.30), for the mass transport streamfunction, ψ, and the interface height, ζ_*, become

$$\psi_{xx} - \frac{1}{\delta_B}\psi_x - (\gamma + l^2)\psi = \gamma H_1 \zeta_*, \tag{4.31}$$

$$\zeta_{*_{xx}} + \frac{1}{\delta_B}\frac{H_1}{H_2}\zeta_{*_x} - \left(\frac{\mathcal{L}}{B_u H} + l^2 + \gamma\frac{H_1}{H_2}\right)\zeta_* = \frac{\mathcal{L}}{H_2}\gamma\psi, \tag{4.32}$$

where

$$\frac{1}{\delta_B} = \frac{H_{T_x}}{H_T}, \quad \gamma = \frac{l}{\delta_B \sigma}, \quad \mathcal{L} = (1-\sigma^2).$$

Define $\epsilon = \sqrt{B_u} << 1$ and expand the variables as

$$\psi = \psi_0 + \epsilon\psi_1 + \epsilon^2\psi_2 + \ldots,$$

$$\zeta_* = \epsilon^m(\zeta_0 + \epsilon\zeta_1 + \epsilon^2\zeta_2 + \ldots),$$

$$\sigma = \sigma_0 + \epsilon\sigma_1 + \epsilon^2\sigma_2 + \ldots,$$

so that

$$\mathcal{L} = 1 - \sigma_0^2 - 2\epsilon\sigma_0\sigma_1 + \mathcal{O}(\epsilon^2),$$

$$\gamma = \frac{l}{\delta_B}(\sigma_0^{-1} - \epsilon\sigma_1\sigma_0^{-2} + \mathcal{O}(\epsilon^2).$$

Plugging the expanded variables into the coupled equations (4.31) and (4.32) gives

$$[\psi_0 + \epsilon\psi_1 + \ldots]_{xx} - \frac{1}{\delta_B}[\psi_0 + \epsilon\psi_1 + \ldots]_x - \left(\gamma_0 + \epsilon\gamma_0\frac{\sigma_1}{\sigma_0} + l^2\right)[\psi_0 + \epsilon\psi_1 + \ldots]$$
$$= \epsilon^m\left(\gamma_0 - \epsilon\gamma_0\frac{\sigma_1}{\sigma_0}\right)H_1[\zeta_0 + \epsilon\zeta_1 + \ldots], \quad (4.33)$$

$$[\zeta_0 + \epsilon\zeta_1 + \ldots]_{xx} + \frac{1}{\delta_B}\frac{H_1}{H_2}[\zeta_0 + \epsilon\zeta_1 + \ldots]_x$$
$$-\left(\frac{1 - \sigma_0^2 - 2\epsilon\sigma_0\sigma_1}{B_u\bar{H}} + l^2 + (\gamma_0 - \epsilon\gamma_0\frac{\sigma_1}{\sigma_0})\frac{H_1}{H_2}\right)[\zeta_0 + \epsilon\zeta_1 + \ldots]$$
$$= \frac{\epsilon^{-m}}{H_2}\left((1 - \sigma_0^2)\gamma_0 - \epsilon(1 + \sigma_0^2)\frac{\sigma_1}{\sigma_0}\gamma_0\right)[\psi_0 + \epsilon\psi_1 + \ldots], \quad (4.34)$$

where $\gamma_0 = \frac{l}{\delta_B\sigma_0}$.

Multiplying (4.34) by ϵ^2 makes it easy to see that the lowest order balances for this equation are

$\mathcal{O}(\epsilon^0)$:

$$-\frac{1}{\bar{H}}(1 - \sigma_0^2)\zeta_0 = \frac{\epsilon^{2-m}}{H_2}(1 - \sigma_0^2)\gamma_0\psi_0, \quad (4.35)$$

$\mathcal{O}(\epsilon^1)$:

$$\frac{2}{\bar{H}}(\sigma_0\sigma_1)\zeta_0 - \frac{1}{\bar{h}}(1 - \sigma_0^2)\zeta_1 = \frac{\epsilon^{2-m}}{H_2}\left((1 - \sigma_0^2)\gamma_0\psi_1 - (1 + \sigma_0^2)\frac{\sigma_1}{\sigma_0}\gamma_0\psi_0\right). \quad (4.36)$$

Thus, from (4.35), it is apparent that $\zeta_0 = \mathcal{O}(\epsilon^2\psi_0)$, i.e. $m = 2$, and the baroclinic perturbations of the motion are much smaller than the associated barotropic basic state.

The lowest order balances of (4.33) are then

$\mathcal{O}(\epsilon^0)$:

$$\psi_{0_{xx}} - \frac{1}{\delta_B}\psi_{0_x} - (\gamma_0 + l^2)\psi_0 = 0, \quad (4.37)$$

$\mathcal{O}(\epsilon^1)$:

$$\psi_{1_{xx}} - \frac{1}{\delta_B}\psi_{1_x} - (\gamma_0 + l^2)\psi_1 = -\gamma_0\frac{\sigma_1}{\sigma_0}\psi_0. \quad (4.38)$$

The idealized model topography (4.1) is now incorporated into (4.33) so that the solution to (4.37) becomes

$$\psi_0(x) = \begin{cases} f_1 e^{l(x+L_1)}, & -\infty < x \leq -L_1 \\ e^{-\alpha_1 x}(c_1 \cos(\beta_1 x) + c_2 \sin(\beta_1 x)), & -L_1 \leq x \leq 0 \\ e^{\alpha_2 x}(d_1 \cos(\beta_2 x) + d_2 \sin(\beta_2 x)), & 0 \leq x \leq L_2 \\ f_2 e^{-l(x-L_2)}. & L_2 \leq x < \infty \end{cases} \tag{4.39}$$

Note that (4.39) is identical to the solution to the nondivergent barotropic ridge waves found in Chapter 2.

The solution to (4.38) must now be determined to find the perturbation effects of the baroclinic component on the barotropic solution. In the flat region to the west of the ridge ($-\infty < x \leq -L_1$), $H_{T_x} = 0$ and (4.38) becomes

$$\psi_{1_{xx}} - l^2 \psi_1 = 0. \tag{4.40}$$

The solution in this region that satisfies the condition that $\psi_1 \to 0$ as $x \to -\infty$ is

$$\psi_1 = g_1 e^{l(x+L_1)}, \tag{4.41}$$

and the waves are trapped to the ridge.

In the flat region to the east of the ridge ($L_2 \leq x < \infty$), $H_{T_x} = 0$ and (4.38) becomes

$$\psi_{1_{xx}} - l^2 \psi_1 = 0. \tag{4.42}$$

The solution in this region that satisfies the condition that $\psi_1 \to 0$ as $x \to \infty$ is

$$\psi_1 = g_2 e^{-l(x-L_2)}, \tag{4.43}$$

and these waves are also trapped to the ridge.

Over the western slope of the ridge ($-L_1 \leq x < 0$), (4.38) becomes

$$\begin{aligned} \psi_{1_{xx}} + 2\alpha_1 \psi_{1_x} - (\gamma_1 + l^2)\psi_1 &= -\frac{\sigma_1}{\sigma_0}\gamma_1 \psi_0 \\ &= -\frac{\sigma_1}{\sigma_0}\gamma_1 e^{-\alpha_1}(c_1 \cos(\beta_1 x) + c_2 \sin(\beta_1 x)), \end{aligned} \tag{4.44}$$

where $\gamma_1 = -2\alpha_1 \frac{l}{\sigma_0}$.

The general solution to this nonhomogeneous second-order differential equation is

$$\psi_1 = e^{-\alpha_1 x}\left(\cos(\beta_1 x) + c_2 \sin(\beta_1 x) + \frac{\sigma_1 \gamma_1}{\sigma_0 \beta_1}\mathcal{F}_2\right), \tag{4.45}$$

where

$$\begin{aligned}\mathcal{F}_2 = &-\sin(\beta_1 x)\left[c_1\left(\frac{x}{2} + \frac{\sin(2\beta_1 x)}{4\beta_1}\right) - c_2\left(\frac{\cos(2\beta_1 x)}{4\beta_1}\right)\right] \\ &-\cos(\beta_1 x)\left[c_1\left(\frac{\cos(2\beta_1 x)}{4\beta_1}\right) - c_2\left(\frac{x}{2} - \frac{\sin(2\beta_1 x)}{4\beta_1}\right)\right].\end{aligned} \tag{4.46}$$

Over the eastern slope of the ridge ($0 < x \leq L_2$), (4.38) becomes

$$\begin{aligned}\psi_{1_{xx}} - 2\alpha_2 \psi_{1_x} - (\gamma_2 + l^2)\psi_1 &= -\frac{\sigma_1}{\sigma_0}\gamma_2 \psi_0 \\ &= -\frac{\sigma_1}{\sigma_0}\gamma_2 e^{\alpha_2}(d_1 \cos(\beta_2 x) + d_2 \sin(\beta_2 x)),\end{aligned} \tag{4.47}$$

where $\gamma_2 = 2\alpha_2 \frac{l}{\sigma_0}$.

The general solution to this nonhomogeneous second-order differential equation is

$$\psi_1 = e^{\alpha_2 x}\left(d_1 \cos(\beta_2 x) + d_2 \sin(\beta_2 x)) + \frac{\sigma_1 \gamma_2}{\sigma_0 \beta_2}\mathcal{F}_3\right), \tag{4.48}$$

where

$$\begin{aligned}\mathcal{F}_3 = &-\sin(\beta_2 x)\left[d_1\left(\frac{x}{2} + \frac{\sin(2\beta_2 x)}{4\beta_2}\right) - d_2\left(\frac{\cos(2\beta_2 x)}{4\beta_2}\right)\right] \\ &-\cos(\beta_2 x)\left[d_1\left(\frac{\cos(2\beta_2 x)}{4\beta_2}\right) - d_2\left(\frac{x}{2} - \frac{\sin(2\beta_2 x)}{4\beta_2}\right)\right].\end{aligned} \tag{4.49}$$

Pressure and the normal transport are continuous in x which implies the jump conditions

$$[\psi_1(x)] = 0 \quad \text{at} \quad x = -L_1, 0, L_2, \tag{4.50}$$

$$[\psi_{1_x}(x)] = 0 \quad \text{at} \quad x = -L_1, 0, L_2. \tag{4.51}$$

Since ψ_1 is continuous in x (4.41), (4.45), (4.48), and (4.43) may be matched at $x = -L_1$, 0, and L_2 to show that

$$g_1 = \left((c_1 \cos(\beta_1 L_1) - c_2 \sin(\beta_1 L_1)) + \frac{\sigma_1 \gamma_1}{\sigma_0 \beta_1} \mathcal{F}_1 \right) e^{\alpha_1 L_1}, \tag{4.52}$$

$$d_1 = \frac{1 - \frac{\sigma_1 \gamma_1}{4\sigma_0 \beta_1^2}}{1 - \frac{\sigma_1 \gamma_2}{4\sigma_0 \beta_2^2}} c_1, \tag{4.53}$$

$$g_2 = \left((d_1 \cos(\beta_2 L_2) + d_2 \sin(\beta_2 L_2)) + \frac{\sigma_1 \gamma_2}{\sigma_0 \beta_2} \mathcal{F}_4 \right) e^{\alpha_2 L_2}, \tag{4.54}$$

respectively, where

$$\begin{aligned} \mathcal{F}_1 = {} & \sin \beta_1 L_1 \left[c_1 \left(\frac{-L_1}{2} - \frac{\sin(2\beta_1 L_1)}{4\beta_1} \right) - c_2 \left(\frac{\cos(2\beta_1 L_1)}{4\beta_1} \right) \right] \\ & - \cos \beta_1 L_1 \left[c_1 \left(\frac{\cos(2\beta_1 L_1)}{4\beta_1} \right) - c_2 \left(\frac{-L_1}{2} + \frac{\sin(2\beta_1 L_1)}{4\beta_1} \right) \right], \end{aligned} \tag{4.55}$$

$$\begin{aligned} \mathcal{F}_4 = {} & - \sin \beta_2 L_2 \left[d_1 \left(\frac{L_2}{2} + \frac{\sin(2\beta_2 L_2)}{4\beta_2} \right) - d_2 \left(\frac{\cos(2\beta_2 L_2)}{4\beta_2} \right) \right] \\ & - \cos \beta_2 L_2 \left[d_1 \left(\frac{\cos(2\beta_2 L_2)}{4\beta_2} \right) - d_2 \left(\frac{L_2}{2} - \frac{\sin(2\beta_2 x)}{4\beta_2} \right) \right]. \end{aligned} \tag{4.56}$$

The derivative of ψ_1 with respect to x is then

$$\psi_1(x) = \begin{cases} l \left(c_1 \cos \beta_1 L_1 - c_2 \sin \beta_1 L_1 + \frac{\sigma_1 \gamma_1}{\sigma_0 \beta_1} \mathcal{F}_1 \right) e^{\alpha_1 L_1} e^{l(x+L_1)}, & -\infty < x \leq -L_1 \\ -\alpha_1 (c_1 \cos(\beta_1 x) + c_2 \sin(\beta_1 x) + \frac{\sigma_1 \gamma_1}{\sigma_0 \beta_1} \mathcal{F}_2) e^{-\alpha_1 x} & \\ \quad + \beta_1 (c_2 \cos(\beta_1 x) - c_1 \sin(\beta_1 x)) e^{-\alpha_1 x} + \frac{\sigma_1 \gamma_1}{\sigma_0 \beta_1} \mathcal{F}_{2_x}, & -L_1 \leq x \leq 0 \\ \alpha_2 (d_1 \cos(\beta_2 x) + d_2 \sin(\beta_2 x) + \frac{\sigma_1 \gamma_2}{\sigma_0 \beta_2} \mathcal{F}_3) e^{\alpha_2 x} & \\ \quad + \beta_2 (d_2 \cos(\beta_2 x) - d_1 \sin(\beta_1 x)) e^{\alpha_2 x} + \frac{\sigma_1 \gamma_2}{\sigma_0 \beta_2} \mathcal{F}_{3_x}, & 0 \leq x \leq L_2 \\ -l \left(d_1 \cos \beta_2 L_2 - d_2 \sin \beta_2 L_2 + \frac{\sigma_1 \gamma_2}{\sigma_0 \beta_2} \mathcal{F}_4 \right) e^{\alpha_2 L_2} e^{-l(x-L_2)}, & L_2 \leq x < \infty \end{cases} \tag{4.57}$$

where

$$\begin{aligned} \mathcal{F}_{2_x} = {} & - \sin \beta_1 x \left[c_1 \left(\frac{x}{2} + \frac{\sin(2\beta_1 x)}{4\beta_1} \right) - c_2 \left(\frac{\cos(2\beta_1 x)}{4\beta_1} \right) \right] \\ & - \cos \beta_1 x \left[c_1 \left(\frac{\cos(2\beta_1 x)}{4\beta_1} \right) - c_2 \left(\frac{x}{2} - \frac{\sin(2\beta_1 x)}{4\beta_1} \right) \right], \end{aligned} \tag{4.58}$$

$$\begin{aligned} \mathcal{F}_{3_x} = {} & - \sin \beta_2 x \left[d_1 \left(\frac{x}{2} + \frac{\sin(2\beta_2 x)}{4\beta_2} \right) - d_2 \left(\frac{\cos(2\beta_2 x)}{4\beta_2} \right) \right] \\ & - \cos \beta_2 x \left[d_1 \left(\frac{\cos(2\beta_2 x)}{4\beta_2} \right) - d_2 \left(\frac{x}{2} - \frac{\sin(2\beta_2 x)}{4\beta_2} \right) \right]. \end{aligned} \tag{4.59}$$

Since ψ_{1_x} is also continuous in x, (4.57) can be matched at $x = -L_1$, 0,and L_2 to get

$$c_1\left((\alpha_1 + l)\cos(B_1)\right) - \beta_1 \sin(B_1)) - c_2\left((\alpha_1 + l)\sin(B_1)\right) - \beta_1 \cos(B_1))$$
$$+\frac{\sigma_1\gamma_1}{\sigma_0\beta_1}(l\mathcal{F}_1 + \alpha_1\mathcal{F}_2 - \mathcal{F}_{2_x}) = 0, \quad (4.60)$$
$$c_1(\alpha_1 + \lambda\alpha_2) - c_2\beta_1 + d_2\beta_2 = 0, \quad (4.61)$$
$$-c_1\lambda\left((\alpha_2 + l)\cos(B_2)\right) - \beta_2 \sin(B_2)) - d_2\left((\alpha_2 + l)\sin(B_2)\right) + \beta_2 \cos(B_2))$$
$$-\frac{\sigma_1\gamma_2}{\sigma_0\beta_2}(\alpha_2\mathcal{F}_3 + l\mathcal{F}_4 + \mathcal{F}_{3_x}) = 0, \quad (4.62)$$

where

$$\lambda = \frac{1 - \frac{\sigma_1\gamma_1}{4\sigma_0\beta_1^2}}{1 - \frac{\sigma_1\gamma_2}{4\sigma_0\beta_2^2}}. \quad (4.63)$$

Setting the determinant of the matrix of coefficients for this set of equations to zero determines the dispersion relation for the perturbation frequency, σ_1, for a given l as everything else in the equations is known. The effect of σ_1 on the barotropic dispersion curve for a generic ridge is shown in Figure 4-2. The frequencies increase as ϵ increases, but for very weak stratification the effect is small.

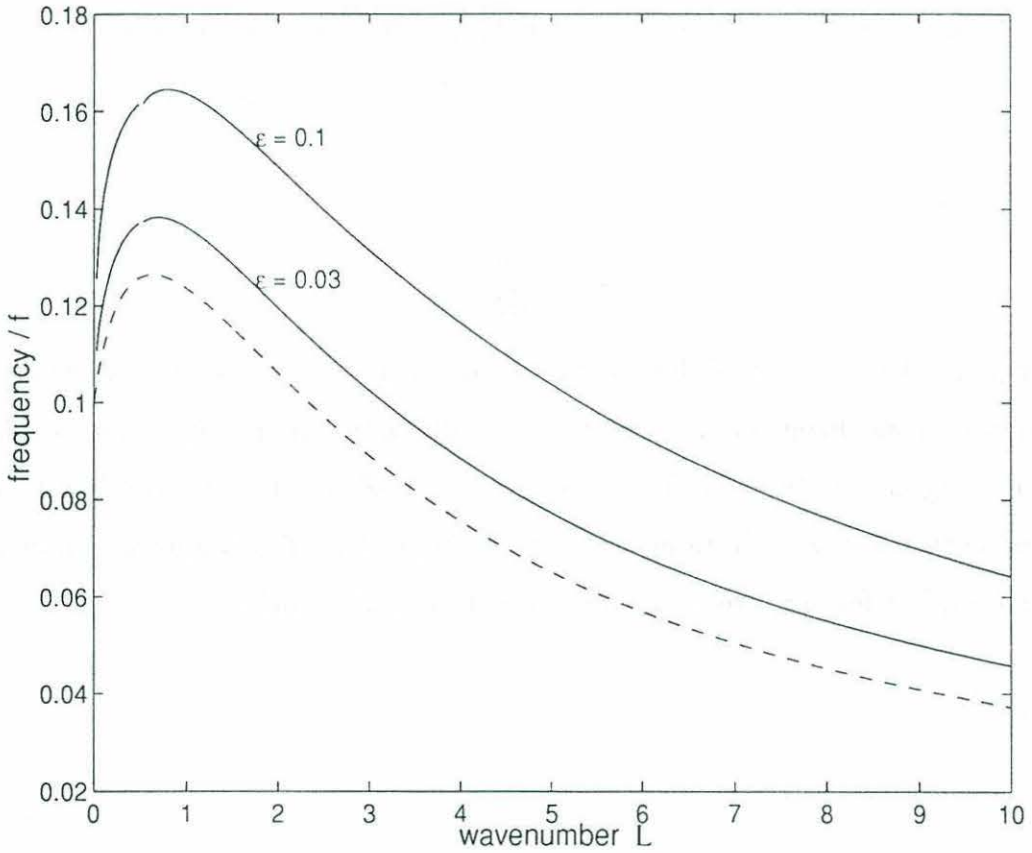

Figure 4-2: The nondivergent ridge wave dispersion curve including the perturbation ($\sigma = \sigma_0 + \epsilon\sigma_1$) for the two values of ϵ shown. The basic barotropic state is shown by the dashed line. The ridge is described by $L_1 = 1$, $L_2 = 0.5$, $\alpha_1 = 0.2$, and $\alpha_2 = 0.2$.

4.3 Vertical trapping

To examine the extent of bottom trapping, the velocity fields in each layer are compared. Substituting the expanded form of the variables ψ and ζ into (4.21) - (4.24) produces

$$v_1 = \frac{\psi_{0_x}}{H_T} + \epsilon\frac{\psi_{1_x}}{H_T} + \epsilon^2\frac{\psi_{2_x}}{H_T} - \frac{H_2}{H_T(1-\sigma_0^2)}(\zeta_{0_x} - \zeta_{0_{yt}}), \tag{4.64}$$

$$v_2 = \frac{\psi_{0_x}}{H_T} + \epsilon\frac{\psi_{1_x}}{H_T} + \epsilon^2\frac{\psi_{2_x}}{H_T} + \frac{H_1}{H_T(1-\sigma_0^2)}(\zeta_{0_x} - \zeta_{0_{yt}}), \tag{4.65}$$

$$u_1 = -\frac{\psi_{0_y}}{H_T} - \epsilon\frac{\psi_{1_y}}{H_T} - \epsilon^2\frac{\psi_{2_y}}{H_T} + \frac{H_2}{H_T(1-\sigma_0^2)}(\zeta_{0_{xt}} - \zeta_{0_y}), \tag{4.66}$$

$$u_2 = -\frac{\psi_{0_y}}{H_T} - \epsilon\frac{\psi_{1_y}}{H_T} - \epsilon^2\frac{\psi_{2_y}}{H_T} - \frac{H_1}{H_T(1-\sigma_0^2)}(\zeta_{0_{xt}} - \zeta_{0_y}). \tag{4.67}$$

Because it has been determined that $\zeta_0 = \mathcal{O}(\epsilon^2)$, the lowest order velocity balances of each layer are

$\mathcal{O}(\epsilon^0)$:

$$v_1^{(0)} = \frac{\psi_{0_x}}{H_T}, \quad u_1^{(0)} = -\frac{\psi_{0_y}}{H_T},$$
$$v_2^{(0)} = \frac{\psi_{0_x}}{H_T}, \quad u_2^{(0)} = -\frac{\psi_{0_y}}{H_T},$$

$\mathcal{O}(\epsilon^1)$:

$$v_1^{(1)} = \frac{\psi_{1_x}}{H_T}, \quad u_1^{(1)} = -\frac{\psi_{1_y}}{H_T},$$
$$v_2^{(1)} = \frac{\psi_{1_x}}{H_T}, \quad u_2^{(1)} = -\frac{\psi_{1_y}}{H_T},$$

$\mathcal{O}(\epsilon^2)$:

$$v_1^{(2)} = \frac{\psi_{2_x}}{H_T} - \frac{H_2}{H_T(1-\sigma_0^2)}(\zeta_{0_x} - l\sigma_0\zeta_0), \tag{4.68}$$

$$u_1^{(2)} = -\frac{\psi_{2_y}}{H_T} + \frac{H_2}{H_T(1-\sigma_0^2)}(\zeta_{0_x} + il\zeta_0), \tag{4.69}$$

$$v_2^{(2)} = \frac{\psi_{2_x}}{H_T} + \frac{H_1}{H_T(1-\sigma_0^2)}(\zeta_{0_x} - l\sigma_0\zeta_0), \tag{4.70}$$

$$u_2^{(2)} = -\frac{\psi_{1_y}}{H_T} - \frac{H_1}{H_T(1-\sigma_0^2)}(\zeta_{0_x} + il\zeta_0). \tag{4.71}$$

Note that the terms for v_1 and v_2 are identical except for the last terms in (4.69) and (4.71) as is the case for the terms for u_1 and u_2. Thus, any trapping of velocities

will be due to the second $\mathcal{O}(\epsilon^2)$ term in the expressions for velocity. The structure of the velocities from the northward moving wave is shown in Figure 4-3 for $B_u = 0.1$. The velocities in the lower layer have a larger magnitude than the velocities in the upper layer over the western slope and a slightly smaller magnitude on the eastern slope. The velocities are therefore considered bottom-trapped on the side of the ridge that supports the wave. As stratification decreases, the bottom-trapping becomes weaker and the difference in velocities becomes quite small.

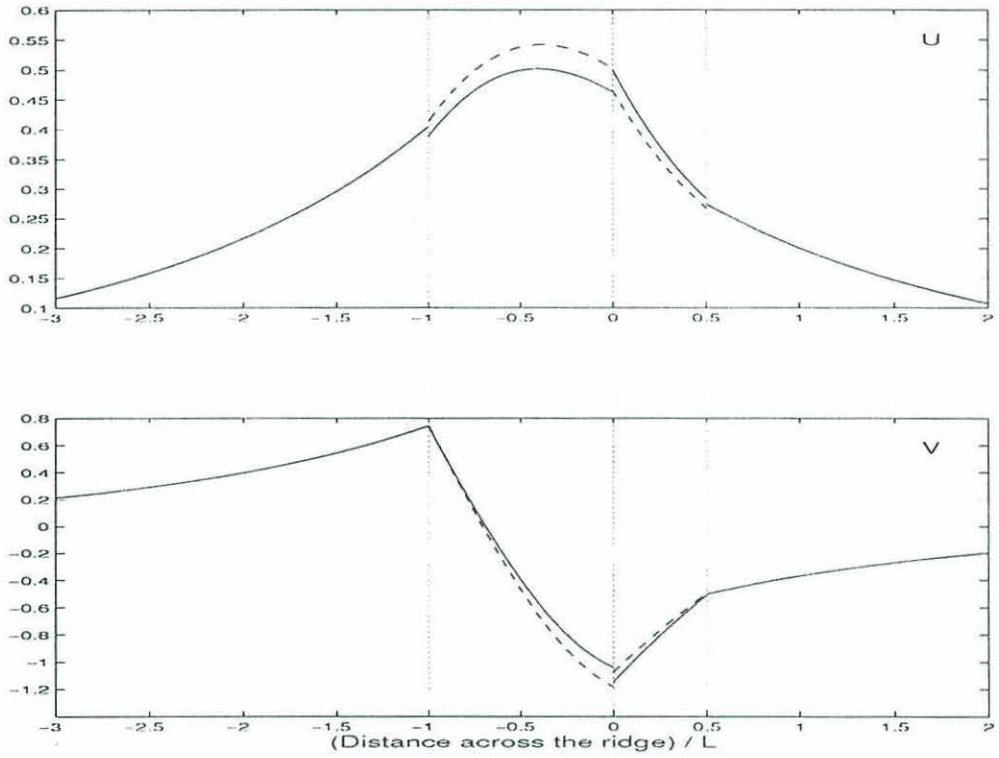

Figure 4-3: Velocity structure across the ridge for a) u and b) v at $t = 1$ and $y = 1$ in both the upper (—) and lower (– –) layers of the two-layer model where $B_u = 0.1$. The ridge is described by $L_1 = 1$, $L_2 = 0.5$, $\alpha_1 = 0.2$, $\alpha_2 = 0.2$ and is shown by the dotted lines.

Chapter 5

Discussion

The goal of this highly idealized study is the exploration of the fundamental characteristics of low-frequency waves trapped to mid-ocean ridge topography. A model for nondivergent barotropic ridge waves was developed in Chapter 2 and the effects of divergence and stratification were incorporated in Chapters 3 and 4, respectively. While it is understood that the along-ridge length scales of the JdFR and other similar ridge segments are a far cry from the infinite ridge approximation used in the previous chapters, a comparison of the observations and the general model results will now be made in order to revisit some of the properties ubiquitous to ridge waves.

5.1 Juan de Fuca Ridge

The basic predictions of the models are supported by observations over the JdFR. The predicted direction of phase propagation over a ridge is observed at the JdFR. Cannon *et al.* (1991) encounter a four-day oscillation with northward propagation over the ridge crest while Chave *et al.* (1989) see southward propagation over the eastern flank of the ridge. It should be noted, however, that the results from the eastern side of the ridge are somewhat complicated. Not only do Chave *et al.* (1989) observe a four-day period that is well outside the range of frequencies that can freely propagate southward along the eastern flank of the JdFR, but an 8-12 day oscillation as well. This second southward propagating wave is observed to the east the ridge's

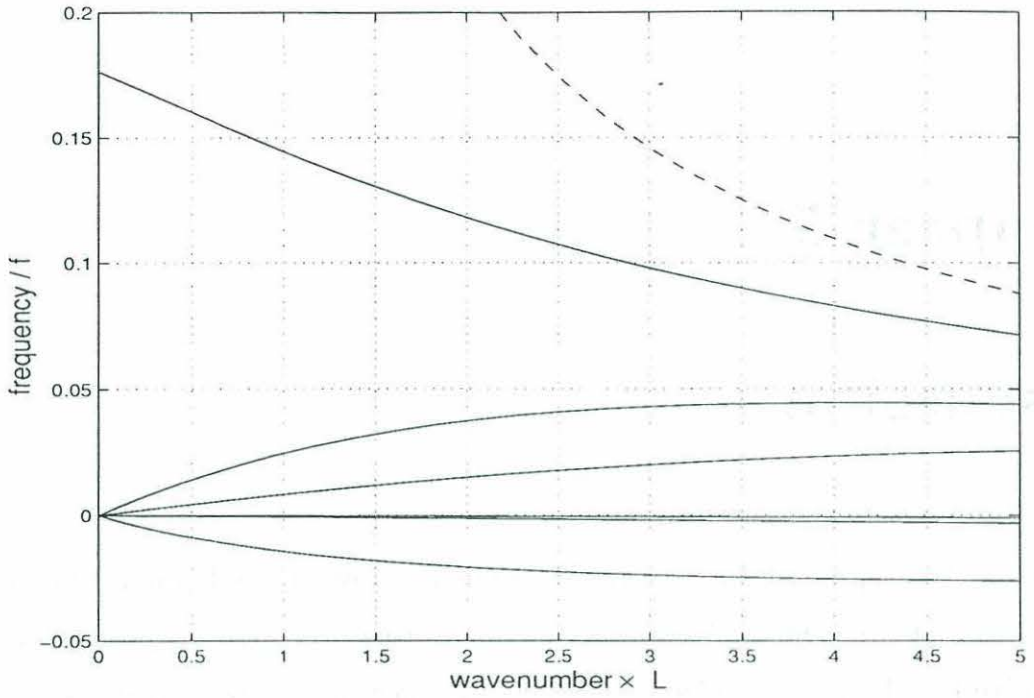

Figure 5-1: The first three modes of the nondivergent barotropic ridge waves over the northern Juan de Fuca Ridge. The topography is shown in Figure 1-4a and is represented nondimensionally by $L_1 = 1$, $L_2 = 0.13$, $\alpha_1 = 0.22$, and $\alpha_2 = 0.32$. The dashed lines represent the frequency cutoff for the modes.

eastern flank. The 8-12 day period is much closer to what the barotropic ridge wave model predicts for the southward propagating waves (6-9 days). Both waves are estimated to have wavelengths of approximately 1000 km.

The barotropic nondivergent dispersion curves for the three JdFR cross section approximations from Figure 1-4 are shown in Figures 5-1 (north), 5-2 (middle), and 5-3 (south). The lowest mode group velocity of the western slope ridge waves does not change sign for the northernmost cross section. It does reverse sign, however, for the the middle and southern sections. The JdFR broadens to the north and the eastern slope gradually diminishes in size. The waves travelling north on the western slope therefore feel less of an opposing topography gradient for the northern section of the ridge segment and behave more like isolated shelf waves than the waves travelling on a ridge modelled by the middle or southern cross sections.

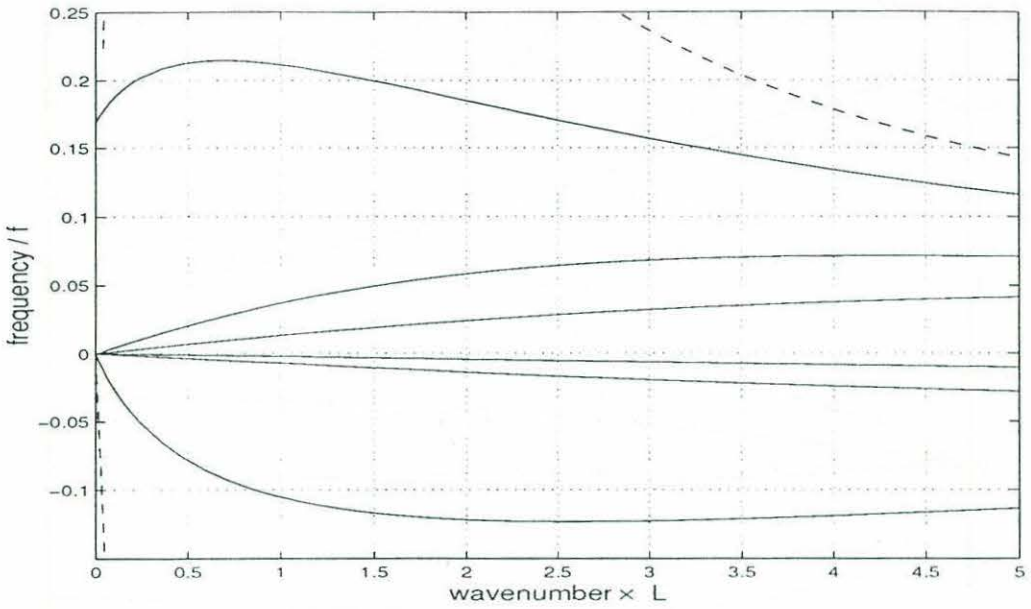

Figure 5-2: The first three modes of the nondivergent barotropic ridge waves over the mid Juan de Fuca Ridge. The topography is shown in Figure 1-4b and is represented nondimensionally by $L_1 = 1$, $L_2 = 0.29$, $\alpha_1 = 0.36$, and $\alpha_2 = 0.65$. The dashed lines represent the frequency cutoff for the modes.

Since the ZGV is important in the interpretation of the subinertial energy peak in the velocity spectra, the divergent model from Chapter 3 is used to ensure a change in sign of the lowest mode group velocity for all three JdFR sections. The divergent dispersion curves for the lowest mode of the western slope waves for ridges described by the three cross sections are shown in Figure 5-4. They are identical to the nondivergent dispersion curves at small wavelengths, but have lower frequencies at the longer wavelengths than their nondivergent counterparts. A maximum possible frequency (the ZGV) can now be found for each of the the three cross sections.

The period and the wavelength of the three ZGV points are listed in Table 5-1. Although the wavelengths of the ZGV waves are between 5 and 10 times the length of the ridge itself, the period of the observed four-day oscillation is seen in the model results.

Cannon and Thomson (1996) observe the four-day oscillation at both ends of the

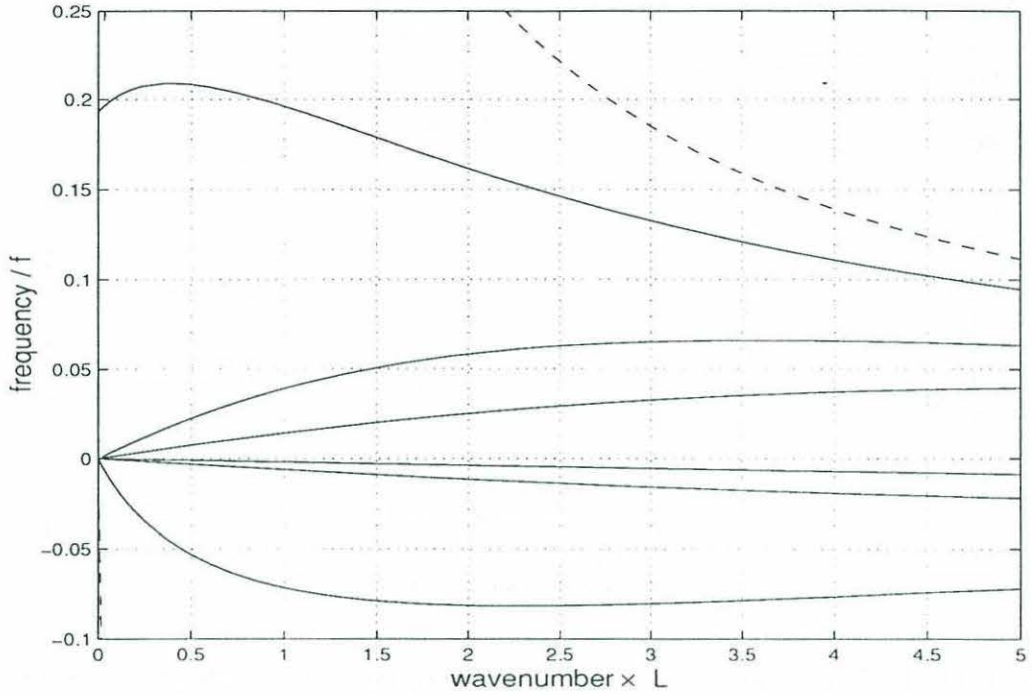

Figure 5-3: The first three modes of the nondivergent barotropic ridge waves over the southern Juan de Fuca Ridge. The topography is shown in Figure 1-4c and is represented nondimensionally by $L_1 = 1$, $L_2 = 0.32$, $\alpha_1 = 0.28$, and $\alpha_2 = 0.35$. The dashed lines represent the frequency cutoff for the modes.

ridge during simultaneous current meter measurements over 280 days in 1984-85 and 260 days in 1986-87. In the 1984-85 observations they find a 30° phase difference in coherence peaks between two moorings separated by about 380 km where the south leads the north. They assume the distance between the moorings is between one and two cycles and determine the wavelength of the oscillations to be 350 km. If the mooring locations were assumed to be less than one cycle apart, the wavelength would be about 4500 km and much closer to the long wavelengths predicted by the model. Similarly, in the 1986-87 observations there was a 90° phase difference between two moorings located approximately 370 km apart. They again assume the distance between the mooring locations was between one and two cycles to get a wavelength of about 300 km. The longer wavelength would then be about 1500 km if the separation distance was assumed to be within the first cycle.

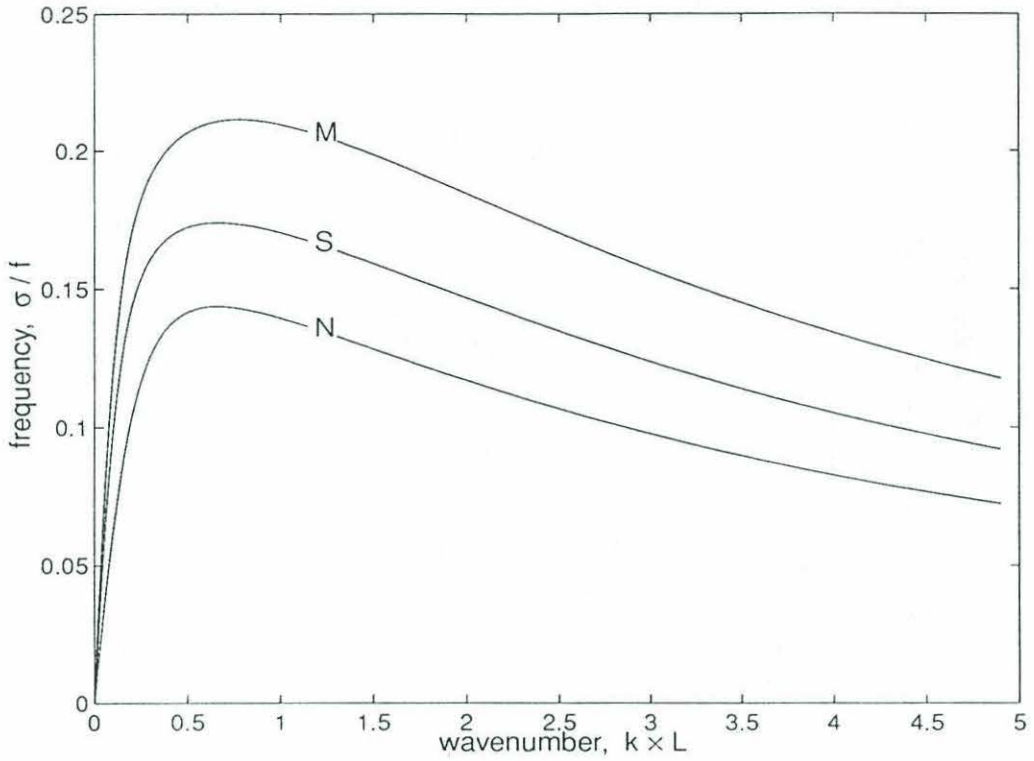

Figure 5-4: The lowest mode of the divergent barotropic ridge waves over the Juan de Fuca Ridge for the northern (N), middle (M), and southern (S) cross sections shown in Figure 1-4.

The structure of the velocity fields is also important. As shown in Figure 2-8, moorings along the crest of the ridge are predicted to see anticyclonic velocity ellipses. Figure 5-5 shows a progressive vector diagram of the depth-averaged velocities seen by the ADCP mooring shown in Figure 1-1 for the 250 m of water column directly over the ridge. A four-day anticyclonic velocity ellipse with inertial oscillations superimposed is quite obvious. As the ridge axis is rotated clockwise about 20° from the north-south direction, the major axis of the ellipse is aligned almost parallel to the ridge.

In determining whether the stratification over the JdFR could also be important for the velocity fields, an average observed stratification of $N^2 = 10^{-6}s^{-2}$ is used to get an expansion coefficient based on the Burger Number $\left(\epsilon = \sqrt{\frac{N^2 H_*^2}{f^2 L^2}}\right)$ of 0.08. Because ϵ is so small, the model predicts very little bottom-trapping. Although

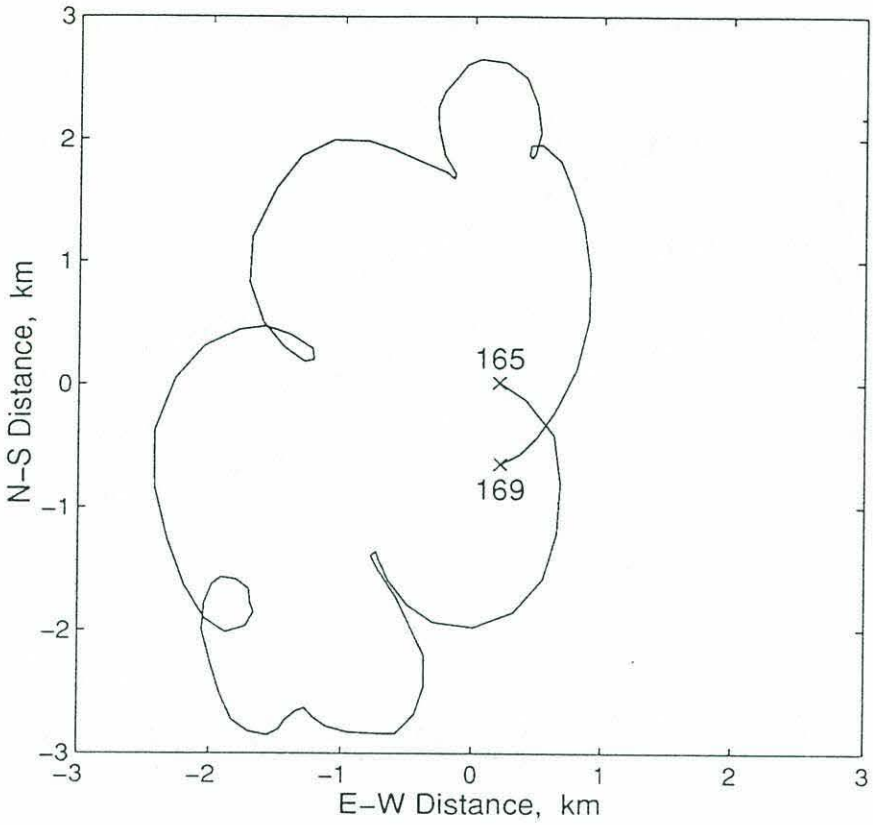

Figure 5-5: Progressive velocity vector diagram of depth-averaged velocities from ADCP moored on Juan de Fuca Ridge from day 165 to day 169.

Figure 1-2 supports the barotropic nature of the oscillation, others have seen a more significant decrease in the amplitude of the signal at greater heights above the ridge crest (Cannon *et al.*, 1991; Thomson *et al.*, 1990).

Table 5.2: JdFR ZGV frequencies and wavelengths

JdFR Cross Section	Period (days)	Wavelength (km)
North	5.1	4400
Mid	3.4	1900
South	4.2	2700

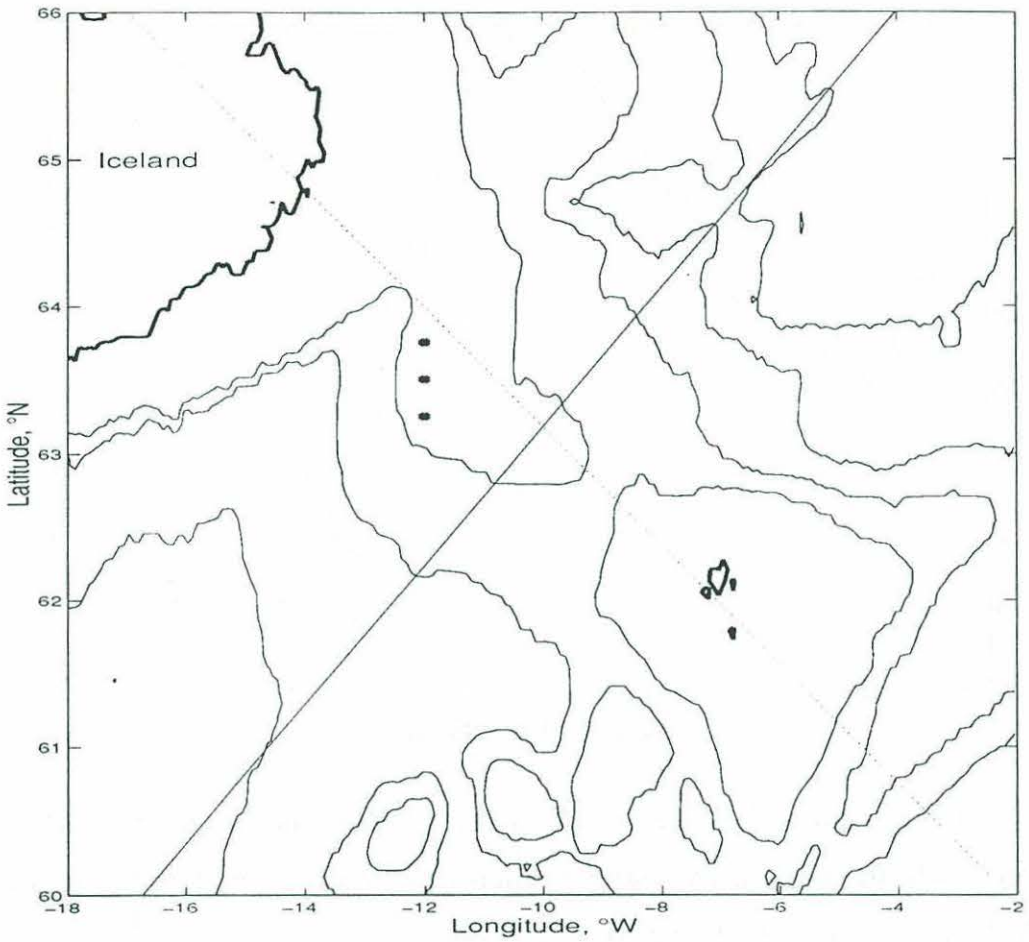

Figure 5-6: The topography of the Iceland-Faeroe Ridge with the 500, 1000, 2000, 3000, and 4000 m isobaths drawn. The 'x's mark the locations of current meter moorings from Miller *et al.* (1996). The dotted line represents the ridge axis and the solid line is the cross section fit by the model topography approximation.

5.2 Iceland-Faeroe Ridge

In addition to the four day oscillation seen in the JdFR records, Miller *et al.* (1996) find a 1.8 day peak in the coherence spectra among current meter moorings along the southern flank of the Iceland-Faeroe Ridge (IFR).

The topography of the IFR is shown in Figure 5-6. This 600 km ridge is much steeper than the JdFR and will support waves with higher frequencies. The to-

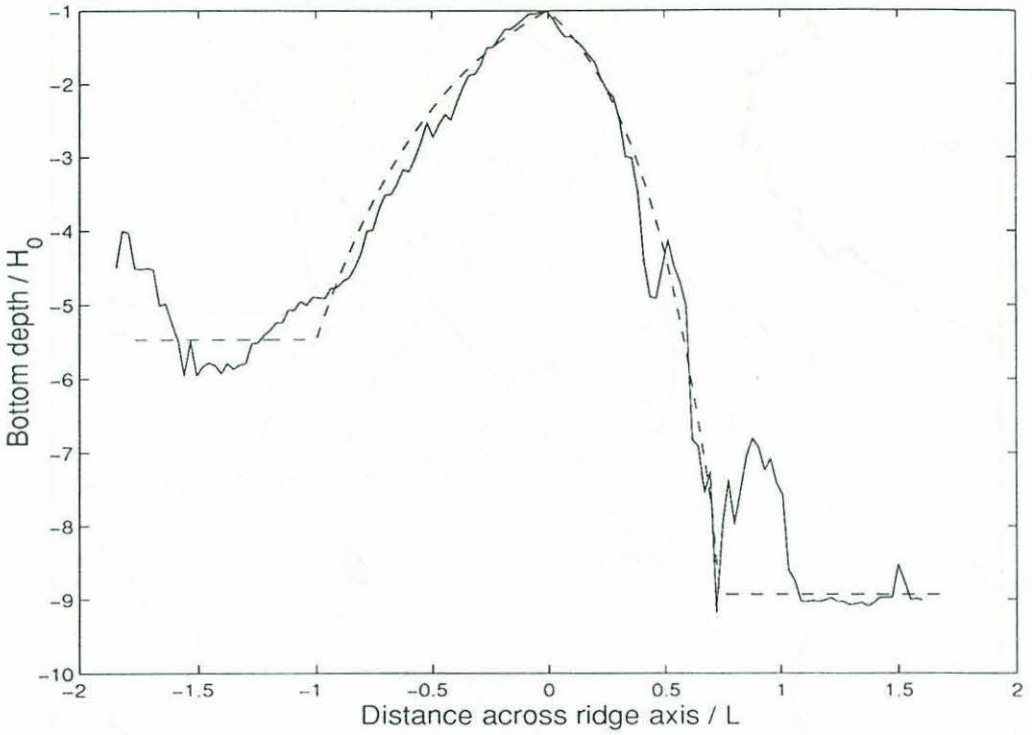

Figure 5-7: The nondimensional cross section of the Iceland-Faeroe Ridge marked in Figure 5-6 (—) fit by the model topography approximation (− −) with the parameters $L_1 = 1.0$, $L_2 = 0.75$, $\alpha_1 = 1.12$, and $\alpha_2 = 1.13$.

pographic approximation (2.7) fit to an IFR cross section is shown in Figure 5-7. Again, although there are small-scale topographic variations on the ridge, the double-exponential depth profile captures the basic trends of the topography.

The divergent barotropic dispersion curve for the lowest mode of the ridge waves supported by the southern flank of the IFR is shown in Figure 5-8. The period of the ZGV predicted by the divergent ridge wave model is about 1.2 days. Miller *et al.* (1997) were able to more accurately predict the observed 1.8 day period by searching for normal modes in the region to the south of the ridge instead of propagating topographically trapped waves along the ridge. They use the nondivergent barotropic shallow water equations over the realistic relief of the ETOPO5 topography (5′ resolution) to predict the occurance of a topographic-Rossby normal mode over the southern flank of the ridge. A comparison of both model results and the

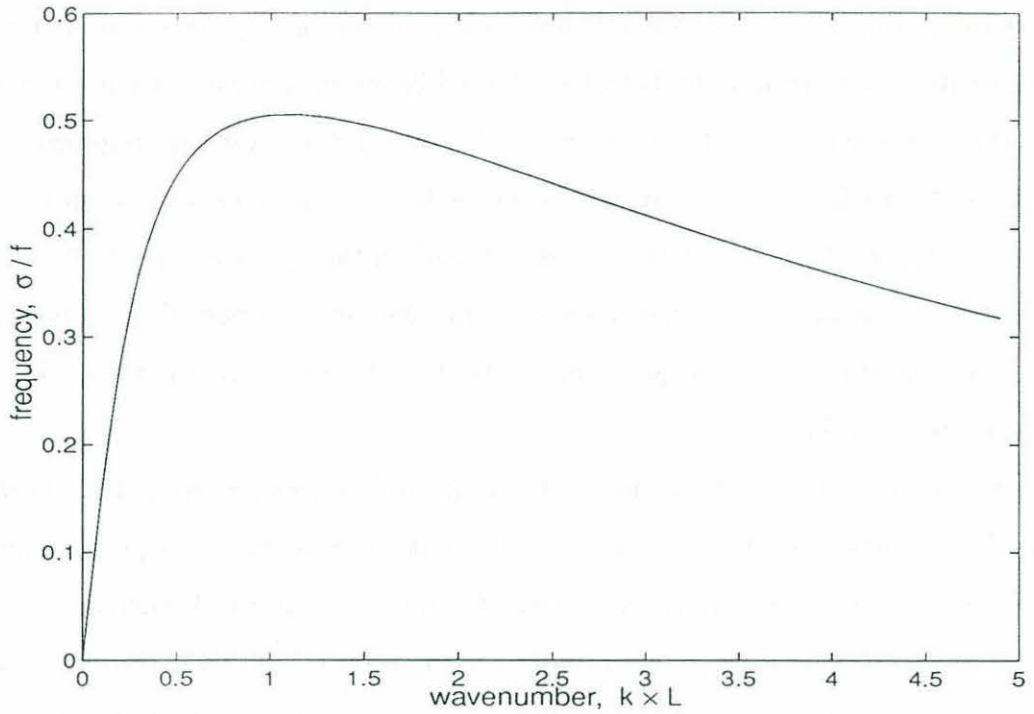

Figure 5-8: The lowest mode of the divergent barotropic ridge wave for the Iceland-Faeroe Ridge cross section shown in Figure 5-7.

observations suggests that modal resonance may be the primary contribution to the observed spectral peak over the IFR instead of an accumulation of energy due to the existence of a ZGV.

5.3 Final Remarks

The complicated structure of the Juan de Fuca Ridge must be commented upon. It is a 450 km ridge segment of a much larger mid-ocean ridge and is offset from other segments to the north and south. In addition, it has several smaller discontinuities along its own length. Such irregular topography provides many difficulties for the analysis of the trapped topographic waves.

If the four-day peak in the velocity spectra is due to a zero group velocity in the characteristic dispersion of the trapped oscillations as described in the previous

chapters, the question of whether the long waves can propagate past the offsets along the entire ridge length is left unresolved. If the waves cannot get by the offsets between ridge segments, the peak may be better explained by waves propagating around the ridge so that a resonance is established when the distance around the ridge segment is equivalent to an integral number of wavelengths. Oscillations would propagate northward on the western ridge flank and southward on the eastern ridge flank in this case as well. It must be noted again, however, that the four-day period observed over the JdFR is outside than the range of periods that could freely propagate southward along the eastern flank.

Luther (1995) points out that one of the major differences between the two processes is the potential for energy to propagate. If the waves are propagating energy along ridge segments and exciting resonances on adjacent sections, disturbances have the potential to propagate relatively rapidly for thousands of kilometers. If the existance of a ZGV is behind the spectral peak, the potential for energy propagation along the ridge is unclear.

He also suggests that, while not conclusive, Cannon *et al.*'s (1991) observations of a dominant northward propagation over the ridge crest could provide support for the zero group velocity mechanism if it could be argued that the wave with northward phase propagation is stronger than the southward propagating wave. As shown in the model results, the western slope of the JdFR would support a stronger signal than the eastern slope with higher frequencies due to its greater width.

Although the simple model discussed here does not capture all of the physics involved at mid-ocean ridges, it is a beginning to a better understanding of how low-frequency trapped waves could behave at ridges. The prediction of a ZGV, the phase propagation along the ridge, the structure and sense of the velocity ellipses, and the strength of the bottom-trapping are all important features that have been observed at mid-ocean ridges.

Adding a y-dependence to the topography to allow for shorter ridge segments, including forcing mechanisms and bottom friction, and using observations from longer ridges will only serve to enhance the explanations of these basic characteristics.

References

Allen, S.E., and R.E. Thomson, 1993. Bottom-trapped subinertial motions over midocean ridges in a stratified rotating fluid, *J. Phys. Oceanogr.*, 23, 566-581.

Brink, K.H., 1983. Low-frequency free wave and wind-driven motions over a submarine bank, *J. Phys. Oceanogr.*, 13, 103-116.

Buchwald, V.T., and J.K. Adams, 1968. The propagation of continental shelf waves, *Proc. Roy. Soc. A.*, 305, 235-250.

Cannon, G.A., and R.E. Thomson, 1996. Characteristics of 4-day oscillations trapped by the Juan de Fuca Ridge, *Geophys. Res. Lett.*, 23, 1613-1616.

Cannon, G.A. and D.J. Pashinski, 1992. Moored ADCP measurements near hydrothermal venting, Proc. MTS Conference, *Mar. Tech. Soc.*, Wash., D.C., 542-548.

Cannon, G.A., D.J. Pashinski, and M.R. Lemon, 1991. Middepth flow near hydrothermal venting sites on the southern Juan de Fuca Ridge, *J. Geophy. Res.*, 96, 12,815-12,831.

Chave, A.D., J.H. Filloux, D.S. Luther, L.K. Law, and A. White, 1989. Observations of motional electromagnetic fields during EMSLAB, *J. Geophys. Res.*, 94, 14,153-14,166.

Huthnance, J.M., 1975. On waves trapped over a continental shelf, *J. Fluid Mech.*, 69, 689-704.

Longuet-Higgins, M.S., 1968. Double Kelvin waves with continuous depth profiles, *J. Fluid Mech.*, 34, 49-80.

Luther, D.S., 1995. Waves trapped to discrete topography: existence and implications, *Proc. Eigth Hawaiian Winter Workshop, P. Muller and D. Henderson, eds.*, University of Hawaii at Manoa, 43-56.

Miller, A.J., P.F.J. Lermusiaux, and P.M. Poulain, 1996. A topographic-Rossby mode resonance over the Iceland-Faeroe Ridge, *J. Phys. Oceanogr.*, 2735-2747.

Mysak, L.A., P.H. LeBlond, and W.J. Emery, 1979. Trench Waves, *J. Phys. Oceanogr.*, 9, 1001-1013.

Rhines, P.B., 1969a. Slow oscillations in an ocean of varying depth. Part 1: Abrupt topography, *J. Fluid Mech.*, 37, 161-189.

Rhines, P.B., 1969b. Slow oscillations in an ocean of varying depth. Part 2: Islands and Seamounts, *J. Fluid Mech.*, 37, 191-205.

Stoer, J., and R. Bulirsch, 1991. *Introduction to Numerical Analysis,* 2nd ed. Springer-Verlag.

Thomson, R.E., S.E. Roth, and J. Dymond, 1990. Near-inertial motions over a mid-ocean ridge: Effects of topography and hydrothermal plumes, *J. Geophys. Res.*, 95, 7,261-7,278.